OXFORD CDE

*Journal of Computational Design and Engineering*, 2022, **10**, 139–159

DOI: 10.1093/jcde/qwac126
Advance access publication date: 1 December 2022
**Research Article**

# Frictional contact analysis in a spherical roller bearing

Julio Blanco-Lorenzo [1,*], Sheng Liu[2], Javier Santamaria[1], Paul A. Meehan[2] and Ernesto G. Vadillo[1]

[1]Department of Mechanical Engineering, University of the Basque Country UPV/EHU, Alda. Urquijo s/n, 48013 Bilbao, Spain
[2]School of Mechanical and Mining Engineering, The University of Queensland St Lucia, Brisbane, QLD 4072, Australia
*Corresponding author. E-mail: julio_blanco001@ehu.eus

## Abstract

Numerical analyses of the roller–raceway contact have been carried out in a spherical roller bearing using frictional contact models of different complexity. The models used in the study include an implementation of Kalker's exact contact theory named CECT (Conformal Exact Contact Theory) and detailed Finite Element models. The adequacy of the more simplified contact solutions is assessed by contrasting them with the solutions obtained with the more comprehensive models. Additionally, the use of the exact contact theory, well known in the wheel–rail application, is demonstrated in contact mechanics analyses in rolling bearings, describing relevant details of its implementation for this application. Situations with different normal loads and friction levels have been analysed, and two distinct steady equilibrium configurations of the roller have been identified.

**Keywords:** spherical roller bearings, rolling contact, exact contact theory, Coulomb friction, contact mechanics

## 1. Introduction

The contact conditions between rolling elements and raceways determine to a large extent the operational limits, performance, and life of rolling bearings. Contact mechanics is thus an essential discipline in their design and analysis. Contact analysis methods of different complexity are used depending on the application and purpose of the study. Numerical, grid-based methods generally allow the solution of more general contact problems than analytical methods. Oh and Trachman (1976) and Hartnett (1979) are early examples of numerical solutions of the normal part of 3D contact problems in rolling bearings, based on a discretization of the contact surface. In these works, the potential contact surface was taken as flat, and the contact surfaces were assumed to behave like half-spaces in the normal direction. The computational cost grew rapidly with the refinement of the mesh, as indicated in Oh and Trachman (1976).

Finite Element models (FEM) are also used to obtain numerical contact solutions in rolling bearings. Some examples may be found in Ju *et al.* (2000), Bomidi and Sadeghi (2014), Li *et al.* (2018), and Abdullah *et al.* (2020). Regarding the contact mechanics part of the simulation, these works dealt mainly with the solution of the normal part of the rolling element–raceway contact. In well-lubricated contacts, the tangential stresses are much lower than the normal pressures in the contact. As a result, the precise solution of the normal contact problem has traditionally received more attention than the tangential contact problem in rolling bearings. However, even in well-lubricated contacts, the issues related to the tangential contact problem are relevant in several aspects of rolling bearing design and operation. For instance, the frictional dissipation occurring in the rolling element–raceway contacts may be an important heating source, and call for limiting the operating speed to avoid excessive temperature increase in the bearing. It is also essential for determining the rolling torque, the transmission efficiency, and the wear evolution in the running surfaces of the bearing. This wear may alter the profiles of the contacting surfaces, possibly leading to increased peak normal pressures and reduced rolling contact fatigue (RCF) life, as was shown in Oloffson *et al.* (2000). As indicated in Harris (2001), even though the shear stresses acting on the rolling elements and raceway surfaces in contact are small compared to the normal pressures, they cannot be neglected for the determination of the bearing endurance with regard to fatigue, and in many cases, they are the most significant factor in determining the endurance of a rolling bearing in a given application. By way of example, in Slack and Sadeghi (2010), it was shown how relatively small levels of friction can have a noticeable effect on the propagation pattern of RCF spalls. More recently, it was demonstrated that wear in grease-lubricated spherical roller bearings causes contamination of the grease, which in turn accelerates wear and degradation of the bearing to premature replacement (Pozzebon *et al.*, 2020; Lin & Meehan, 2021). The frictional contact analysis is an essential part of this process.

Frictional contact problems involve a greater difficulty than frictionless contact problems, and simplified contact models are usually employed to facilitate their solution. A commonly used simplifying assumption is that of full slip, wherein the tangential stresses are determined as the normal pressures times a coefficient of friction. This is used for instance in Houpert (1999, 2002) and Leblanc and Nelias (2007), following Jones (1959). As explained in Houpert (1999, 2002), the coefficient of friction is actually variable across the contact (see also Kleckner & Pirvics, 1982). Still, a single value may be used for the full contact provided it is properly calculated according to the average contact pressure and sliding speeds in the contact. Besides the shearing of the lubricant film between the contact surfaces, the possible contribution of the solid direct contact between the surfaces should be

**Received:** July 10, 2022. **Revised:** November 13, 2022. **Accepted:** November 15, 2022

considered. The full slip approach is also commonly used in rigid body dynamics simulations of other mechanical systems involving frictional contacts, to achieve fast computation of the contact resultant forces and moments (Zhuravlev, 1998; Leine & Glocker, 2003; Kireenkov, 2008; Karapetyan, 2009; Kudra & Awrejcewicz, 2013; Zobova, 2019).

The underlying assumption in full slip tangential contact solutions is that the elastic displacement gradients of the contacting surfaces are small in relation to the rigid slip velocities and can be neglected. The surfaces are thus regarded as rigid in the tangential directions of the contact. However, the effects of the tangential elasticity of the bodies may be significant in certain situations, as shown in Halling (1966–67) and Johnson (1985, section 8.5). In these works, the tangential contact problem was solved with the strip theory (Haines & Ollerton, 1963). This consists in dividing the contact patch into parallel strips aligned with the rolling direction and applying in each Carter's plane strain solution for the steady-state rolling contact of two elastically similar bodies (Carter, 1926). The strip theory was also used in Oloffson *et al.* (2000) and Meehan *et al.* (2017) to obtain tangential contact solutions to calculate wear profiles in spherical roller thrust bearings and spherical roller bearings, respectively. This being an analytical solution, its computational costs are much lower than those of numerical methods. On the other hand, it is limited to cases in which the direction of the rigid slip velocities is approximately constant in the rolling direction, as it was initially conceived for situations with pure creepage.

The FASTSIM algorithm (Kalker, 1982) of Kalker's simplified rolling contact theory is another simplified partial slip model for the tangential contact problem, which overcomes the limitation of constant direction of the rigid slip velocities along the contact. The simplification of this model consists in assuming that the elastic tangential displacement in each point in the contact patch depends only on the contact tangential stress at that point. Though commonly used for planar contacts, it may be readily extended to non-planar contacts, provided the assumption of half-space-like elastic behaviour and elastic similarity of the contacting bodies is retained. In this model, the contact patch is divided into a 2D grid of rectangular elements organized in parallel strips aligned with the rolling direction, and the tangential stresses are computed along each strip in a recursive, non-iterative way, moving from the leading to the trailing edge. Therefore, it is still much faster than exact contact models. This model was applied in Legrand and Mondier (1995) and Heras (2018) to different types of ball bearings, seeking to improve the tangential contact solutions obtained with the usual full slip approach.

Generally, when more precise contact solutions are necessary, these have to be obtained numerically. The numerical computation of rolling contact problems was pioneered by Kalker (Kalker, 1979, 1990). He set out the kinematic equations of the contact problem in a Eulerian mesh of the contact surface in which the exact integral relationships between surface stresses and elastic displacements are discretized, and the normal and tangential contact conditions are enforced. The method, known as Kalker's exact contact theory, is aimed at solving contact problems in linear elastostatics and was implemented first in the program DUVOROL and later in the program CONTACT. It is widely known in the railway community and used as a reference to validate simpler contact models. CONTACT has continued being developed by Vollebregt (Vollebregt, 2012, 2020, 2021, 2022), and several authors have programmed their implementations as well, Jin *et al.* (2005), Baeza *et al.* (2011), and Kaiser (2012) being some examples. Wang and Knothe (1993) and Wang *et al.* (2012) are other examples of the application of methods similar to Kalker's exact contact theory for rolling contact problems. In Wang and Knothe (1993), the 2D problem of steady-state rolling of two viscoelastic cylinders was analysed. In Wang *et al.* (2012), 3D steady-state rolling problems with surfaces including micro-irregularities were analysed. The method used here was limited to cases with zero spin.

Some authors classify the exact contact theory as a boundary element method (BEM). Others (e.g., Wang *et al.*, 2012) designate this type of method as a semi-analytical method (SAM), referring to the calculation of the influence coefficients (ICs), which relate surface displacements and stresses. This type of method is indeed commonly used for half-space contact problems, and the half-space ICs are calculated analytically. However, work has been done to extend the exact contact theory to more general geometries with numerically calculated ICs (see e.g., Li, 2002; Vollebregt & Segal, 2014), so the designation of SAM, in this case, is now less appropriate. Here, the designation of 'contact element method' (CEM) will be used for methods like Kalker's exact contact theory, in which just the contact surface is discretized, to distinguish them from the BEM in which the whole contacting solids are discretized. The latter was done e.g., in Abascal and Rodríguez-Tembleque (2007), to solve the structural (global) and the contact (local) problems in a coupled way.

Rolling contact problems have also been studied with BEM. In González and Abascal (1998, 2000), a method was developed to analyse 2D steady rolling contact problems with BEM. This was subsequently extended to 3D, for a deformable wheel on a rigid base in Abascal and Rodríguez-Tembleque (2007), and allowing for the two contacting bodies to be deformable in Rodríguez-Tembleque and Abascal (2010). In the latter work, each body could be meshed with either BEM or FEM. The methodology developed in these references allows for studying coupled structural and contact problems, though the development was aimed at linear elastostatic problems. In González and Abascal (1998, 2000) and in one of the procedures presented in Abascal and Rodríguez-Tembleque (2007), the equilibrium equations were condensed to the degrees of freedom in the potential contact surface, which could be classified as a CEM wherein the ICs are calculated numerically with BEM.

CEM methods are best suited to contact problems not coupled with the structural problem, as is the case in linear elastostatic problems in which the remote loads are not influenced by the specific distribution of contact stresses. In cases in which this premise is not fulfilled due e.g., to large displacements or inelastic material behaviour, FE models are used to get numerical solutions to rolling contact problems. FEM for contact mechanics analyses commonly involves much more degrees of freedom than other contact analysis methods and higher computational costs. In turn, they offer more versatility to include in the analysis complex material behaviour, non-linear geometry, and dynamic effects, for example.

When the rolling is steady state, it is advantageous to set out the problem in a static mesh relative to the motion of the wheel axis of revolution, where the problem can be described in a purely spatial way, without explicit time dependence. In this setting, the displacement fields are decomposed into a part of rigid body motion, which is described in a Eulerian way, and a part of deformation, which is described in a Lagrangian way. This has the advantage of limiting the mesh refinement for detailed contact analysis to the region occupied by the contact patch and of avoiding time stepping. This approach has been used mainly in the tire–road application. The tire undergoes large deformations and has a complex structure and inelastic material behaviour, while the road is commonly assumed to be rigid. This methodology was applied for

2D in Zeid and Padovan (1981), Padovan *et al.* (1984), and Oden and Lin (1986) and extended to 3D in Bass (1987), Padovan (1987), Oden *et al.* (1988), Faria *et al.* (1989, 1992), Nackenhorst (1993), and Le Tallec and Rahier (1994). In this framework, the inertia effects are accounted for, in addition to non-linear geometry and material behaviour. Nackenhorst (Nackenhorst, 1993) noted the relationship between this type of analysis and the Arbitrary Lagrangian Eulerian (ALE) methods (Donea *et al.*, 2004), widely used in fluid–structure interaction problems, among others. Kabe and Koishi (2000), Nackenhorst *et al.* (2000), Hu and Wriggers (2002), Damme *et al.* (2003), Nackenhorst (2004), Ziefle and Nackenhorst (2008), and Rafei *et al.* (2018) are further examples of its development and application in 3D rolling contact problems. In Kabe and Koishi (2000), comparisons between solutions obtained for steady rolling contact with this methodology and with Lagrangian simulations were made, showing the substantial computational advantage of the former.

In Nackenhorst *et al.* (2000) and Damme *et al.* (2003), the application of the ALE formulation for 3D wheel–rail rolling contact analyses was demonstrated, where the two contacting bodies have to be regarded as deformable. As stated in Nackenhorst (2004), future work has to be spent on the development of reliable and efficient numerical algorithms. A difficulty of the ALE formulation for rolling contact problems, which is relevant also in the case of a single deformable body, is that the particle path-dependent variables are not computed inherently. This becomes necessary for the representation of the kinematics of the tangential contact problem and inelastic material behaviour. These issues were addressed in Ziefle and Nackenhorst (2008), and the issue related to the tangential contact problem, viz the computation of the convective term of the contact slip velocities, in Laursen and Stanciulescu (2006) as well. In later works using the ALE formulation (Suwannachit & Nackenhorst, 2013; Behnke & Kaliske, 2015; Draganis *et al.*, 2015; Wollny *et al.*, 2016; Draganis, 2017), thermo-mechanical rolling contact problems have been studied.

For transient rolling contact problems, a total Lagrangian description seems preferable (Wriggers, 2001). Li *et al.* (2008), Zhao and Li (2011), Pletz *et al.* (2014), Vo *et al.* (2014), Zhao *et al.* (2014), and Toumi *et al.* (2016) are examples of Lagrangian 3D wheel–rail rolling contact analyses in which detailed frictional contact solutions were computed with FEM. This type of analysis involves a non-linear time-stepping solution, which is computationally costly. Returning to the rolling bearing application, Heras *et al.* (2017a), Tonazzi *et al.* (2017), Schwack *et al.* (2018), Fallahnezhad *et al.* (2019), and Schwack *et al.* (2021) are examples featuring this type of analysis. A relevant difficulty in rolling contact analyses of rolling bearings with respect to the wheel–rail or tire–road applications is that in many cases more than two contacting bodies have to be modelled. In these works, it was relevant to obtain a detailed solution of the tangential contact problem to get representative friction torques, plastic strains, or wear profiles in the computations.

In this work, the roller–raceway contact is studied in a spherical roller bearing, with partial slip contact models of different complexity, covering the normal and tangential parts of the contact problem. The geometry of the studied bearing is described in Section 2. In Section 3, the used contact models are described. These include the strip theory, the exact contact theory, and FEM. As a novelty with respect to previous works, the use of the exact contact theory is demonstrated in the rolling contact analysis in a rolling bearing. This necessitates a specific adaptation from its original application in the wheel–rail case, which is explained in Section 3.2.2. In Section 4, the results of the numerical studies carried out are presented. On the one hand, rolling contact solutions obtained with the different contact models are compared, discussing the validity of each one for the application. This serves to assess the benefits that may be gained with more comprehensive 3D partial slip contact models, with respect to the usual full slip or simplified 1D partial slip models. Regarding the application of FEM, a detailed assessment of the stationarity of the computed contact solutions is presented, not seen in previous works, which is necessary to achieve valid steady equilibrium solutions in the studied bearing. On the other hand, steady rolling equilibrium configurations of the roller are computed for scenarios with different normal loads and friction levels. This equilibrium study is only possible with a 3D partial slip contact model. Lastly, the main conclusions of the work are compiled in Section 5.

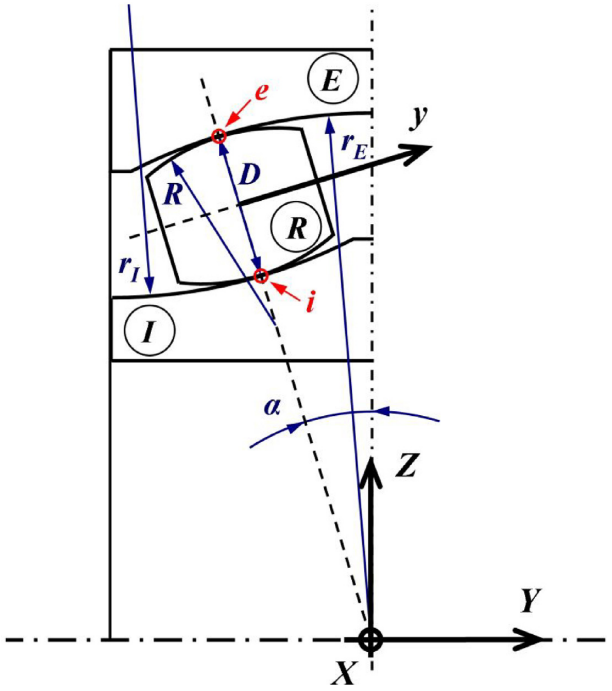


**Figure 1:** Sectional view of the spherical roller bearing.

**Table 1:** Geometric parameters of the spherical roller bearing.

| Parameter | Description | Value |
|---|---|---|
| $D$ (mm) | Roller nominal diameter | 19.8 |
| $r_E$ (mm) | Outer race groove curvature radius | 102.4 |
| $r_I$ (mm) | Inner race groove curvature radius | 103 |
| $R$ (mm) | Roller crown radius | 100.3 |
| $\alpha$ (°) | Nominal contact angle | 11.5 |
| $\alpha_R$ (°) | Roller angle | 0 |

## 2. Description of the Studied Spherical Roller Bearing

The object of this study is a double-row spherical roller bearing with symmetrical barrel-shaped rollers. This is a type of bearing commonly used in railway axles. These bearings have self-aligning and high load-carrying capacity and can carry combined radial and thrust loads (Kleckner & Pirvics, 1982; Harris, 2001). Figure 1 shows a sectional view of the bearing (not to scale), and Table 1 lists its main internal dimensions relevant to the contact

analyses. One-half of the bearing section is shown in the figure, which is symmetrical with respect to the XZ plane. The bearing material is steel, with a Young's modulus $E$ of 207 GPa and a coefficient of Poisson $\nu$ of 0.3.

The resulting roller–raceway contact patches have a high width-to-length ratio (approx. 40) and modest total contact angle variations in the lateral direction. The length refers to the dimension in the rolling direction and the width to the dimension in the lateral direction. The total contact angle variation is around 11° with a normal load on the roller of 5.5 kN. This load has been computed in the most loaded roller for a total radial load of 28.7 kN in the bearing, considering a radial bearing clearance of 0.1 mm.

The following coordinate systems are defined:

1. Bearing {X, Y, Z}: Cartesian coordinate system that rotates with orbital rotation velocity $\omega_m$ following the radial bearing plane containing the central point of the considered roller. Its origin is on the common rotation axis of the inner and outer rings, at the lateral mid-plane of the bearing (between the two rows of rollers). The YZ plane contains the rotation axis of the rings and the roller centre. The Y axis is aligned with the rotation axis of the rings, the Z axis points vertically upwards, and the X axis completes the right-handed coordinate system.
2. Reference roller {x, y, z}: Cartesian coordinate system with origin in the nominal location of the roller centre in the YZ plane, with the y axis aligned with its nominal axis of revolution. It is obtained from the bearing {X, Y, Z} system with a rotation of $\alpha$ around the X axis and displacements of $-r_m \tan(\alpha)$ and $r_m$ along Y and Z. $r_m$ is the pitch radius of the bearing, equal to $(r_E - D/2)\cos(\alpha)$.
3. Roller {u, v, w}: Cartesian coordinate system with origin in the roller centre, which moves solidary to the roller. It is obtained from the {x, y, z} system with the following sequence of rotations and displacements:
   a. $\beta$ tilt rotation around the x axis. After this rotation, a z′ axis is obtained from the z axis.
   b. $\gamma$ yaw or skew rotation around the z′ axis. After this rotation, the orientation of the v axis is defined, which coincides with the roller axis.
   c. $\theta$ pitch rotation around the v axis.
   d. $d_y$ and $d_z$ displacements along the y and z axes.

The tilt and skew rotations of the roller are illustrated in Fig. 2.

The contact of one of the rollers with the inner and outer races is considered. Each body is identified with a letter. *I* is used for the inner ring, *R* for the roller, and *E* for the outer or exterior ring. The nominal contact points of the roller with the inner and outer races are identified in Fig. 1 as 'i' and 'e', respectively. The nominal rolling radii of the rings $r_{\mathrm{roll},I,\mathrm{i}}$ and $r_{\mathrm{roll},E,e}$ are given by equation (1). These are distances in the Z axis from the bearing axis to the inner and outer nominal contact points. The longitudinal curvature radius of each ring at the nominal contact point is equal to the rolling radius divided by $\cos(\alpha)$.

$$r_{\mathrm{roll},I,\mathrm{i}} = r_m - \frac{D}{2}\cos(\alpha)\,;\, r_{\mathrm{roll},E,e} = r_m + \frac{D}{2}\cos(\alpha) \tag{1}$$

In steady rolling, the motion of the roller is composed of an orbital rotation around the global Y axis with angular velocity $\omega_m$ and a pitch rotation around its own v axis with angular velocity $\omega_R$. The theoretical angular velocities for perfect rolling on the nominal contact points are given by equations (2) and (3). In these equations, $\omega_I$ and $\omega_E$ are the rotation velocities of the inner and outer rings (around the global Y axis). Their values are fixed at 476.2 and 0 rpm in this work.

$$\omega_{m,o} = \frac{r_{\mathrm{roll},I,\mathrm{i}}\omega_I + r_{\mathrm{roll},E,e}\omega_E}{r_{\mathrm{roll},I,\mathrm{i}} + r_{\mathrm{roll},E,e}} \tag{2}$$

$$\omega_{R,o} = \frac{-2r_{\mathrm{roll},I,\mathrm{i}}r_{\mathrm{roll},E,e}\left(\omega_I - \omega_E\right)}{D\left(r_{\mathrm{roll},I,\mathrm{i}} + r_{\mathrm{roll},E,e}\right)} \tag{3}$$

Each roller has a mass $m_R$ of 65.6 g and inertia moment about the $u$ axis $I_{R,uu}$ of 5.87 kg.mm$^2$. Together with the kinematic parameters considered, this results in a centrifugal force and a gyroscopic moment of approx. 3 N (along the positive Z axis) and 6 N.mm (along the positive X axis for the roller depicted in Fig. 1), respectively. In the cases analysed in this work, these roller inertia forces are much lower in magnitude than the roller–raceway contact forces, and their effect on the contact solutions is negligible.

## 3. Contact Models

It is aimed to obtain detailed rolling contact solutions for each roller–raceway contact. To this end, different partial slip contact models have been considered in this work. Each of them is described in the following subsections.

The following common assumptions are considered:

1. The bodies are homogeneous, and the material's behaviour is linear elastic and isotropic.
2. Coulomb's friction law is used, with a constant coefficient of friction. This is commonly applied in dry or in boundary lubricated contacts.

The bearing is considered to be radially loaded. The motions of the inner and outer rings are prescribed, as well as the approach between them. The precise motion and position of the roller are to be determined as part of the solution so that the roller complies with steady equilibrium. More precisely, quasi-steady equilibrium configurations of the roller are computed, since the load on the roller changes continuously during its orbital rotation around the bearing.

### 3.1. Strip theory

The strip theory is described in Haines and Ollerton (1963). The necessary geometric and kinematic inputs are obtained under the following assumptions:

1. The roller is considered in its nominal orientation, with neither tilt nor skew.
2. The inner and outer roller–race contact centres are considered to be located in the same rolling circle of the roller.
3. The contact centres, which are prescribed, may be different from the nominal contact points.

The normal contact problem is solved first using the Hertz theory. The same normal load *N* is prescribed for the inner and outer contacts. The crown radius of the roller and groove radii of races are used in the lateral direction and the longitudinal curvature radii of the roller and races at the contact centres in the longitudinal direction. Here, the correction proposed in Blanco-Lorenzo *et al.* (2018) is also applied to the effective lateral curvature, i.e.,

$$B_{\mathrm{corr}} = B + \frac{d}{2r^2} \tag{4}$$

In this equation, $B$ is half the effective lateral curvature, $d$ is the normal approach between two contacting bodies, and $r$ is the mean radius of curvature of the contact surface, which may be approached as the arithmetic mean of the lateral curvature radii

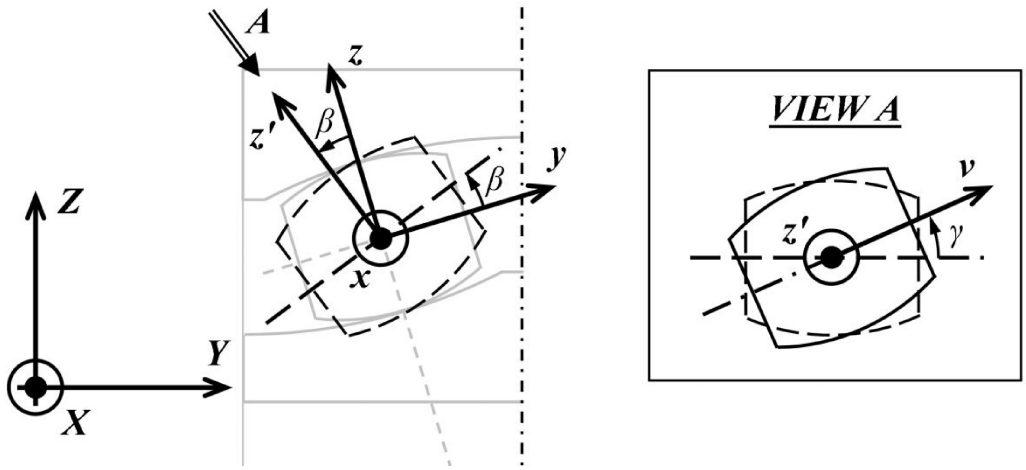


**Figure 2:** Tilt and skew rotations of the roller.

of the two contacting surfaces. In the presently studied case, the effect of this correction, i.e., the second term of equation (4), is negligible.

The tangential contact problem is solved by dividing the contact patch into parallel strips aligned with the x direction and applying Carter's theory (Carter, 1926) independently in each of them. The interaction between different strips is neglected. A pure longitudinal creepage is considered, constant in each strip. The longitudinal rigid slip velocities $w_x$ are calculated as the difference of the relative velocities of the contact patch over each contacting surface. The contact relative velocities $V_{c,j}$ over the surface of each race $j$, $j \in \{I, E\}$, and over the surface of the roller, $V_{c,R}$, are given in equations (5) and (6). These velocities are identical for perfect rolling on the nominal contact points of the inner and outer contacts.

$$V_{c,j} = |\omega_{m/j}|\, r_{\text{roll},j} = |\omega_m - \omega_j|\, r_{\text{roll},j} \tag{5}$$

$$V_{c,R} = |\omega_R|\, r_{\text{roll,R}} \tag{6}$$

In these equations, $r_{\text{roll},j}$ are the rolling radii of each race (measured along the bearing Z axis), and $r_{\text{roll,R}}$ is the rolling radii of the roller (measured along the roller z axis). These are variable in the lateral direction of the contact patch. The longitudinal creepage $\xi$ is thus calculated according to equation (7). The contact velocity $V_c$ is taken as the average of $V_{c,j}$ and $V_{c,R}$.

$$\xi = \frac{V_{c,R} - V_{c,j}}{V_c} = \frac{2\left(V_{c,R} - V_{c,j}\right)}{V_{c,R} + V_{c,j}} \tag{7}$$

For given ring rotation velocities $\omega_I$ and $\omega_E$, $\omega_m$ and $\omega_R$ are iterated until the equilibrium of longitudinal forces and moments around the y axis is satisfied in the roller with the inner and outer contact resultants. Only the tangential contact forces contribute to these equilibrium conditions.

In a strip of maximum normal pressure $p'_{no}$, the normalized creepage $\xi^*$ is calculated according to equation (8). $\mu$ is the coefficient of friction and $E^*$ is calculated as $E/[2(1-\nu^2)]$ for two bodies with the same elastic constants.

$$\xi^* = \frac{E^*}{2\mu p'_{no}}\xi \tag{8}$$

The tangential contact solution in a strip, including the tangential stresses $p_x$ and slip velocities $v_x$, is calculated as a function of the strip values of $\mu p'_{no}$ and $\xi^*$ by Carter's theory:

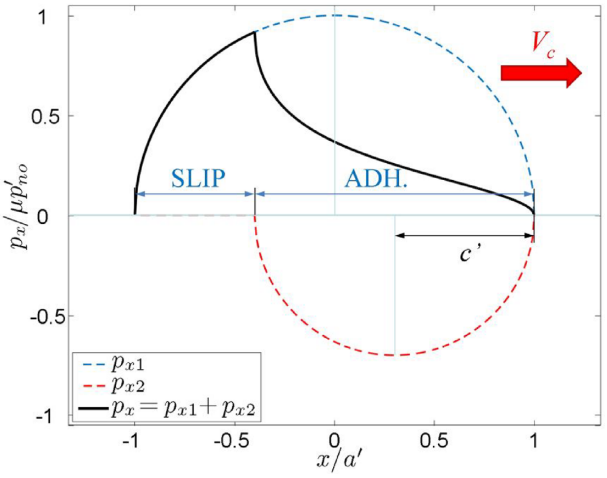


**Figure 3:** Tangential contact stresses in Carter's 2D tangential contact solution.

$$-\text{sgn}(\xi) \times \frac{p_x}{\mu p'_{no}}$$

$$= \begin{cases} \sqrt{1-x'^2} - c'\sqrt{1-\left(\frac{x'-(1-c')}{c'}\right)^2} & \text{for } 1-2c' < x' \le 1 \\ \sqrt{1-x'^2} & \text{for } -1 \le x' \le 1-2c' \end{cases} \tag{9}$$

$$\text{sgn}(\xi) \times \frac{v_x}{V_c}$$

$$= \begin{cases} 0 & \text{for } 1-2c' < x' \le 1 \\ \xi\left(1 + \frac{1}{\xi^*}\left(c' - 1 + \sqrt{(x'-(1-c'))^2 - c'^2}\right)\right) & \text{for } -1 \le x' \le 1-2c' \end{cases} \tag{10}$$

In equations (9) and (10), x′ is equal to the longitudinal distance x from the centre of the strip divided by the half-length of the strip $a'$, and $c'$ the half-length of the adhesion area in the strip $c$ divided by $a'$ (see Fig. 3). $c'$ is equal to $1 - \min(1; |\xi^*|)$. For $|\xi^*| > 1$, the strip is entirely in slip. The resultant longitudinal force in a strip $dF_x$ may be obtained by integrating $p_x$ over the strip. The result is given in equation (11) for a strip of unit width, with $dN$ being the resultant normal force on the strip, equal to $\pi a' p'_{no}/2$.

$$dF_x = -\text{sgn}(\xi) \times \left(1 - c'^2\right) \times \mu \times dN \tag{11}$$

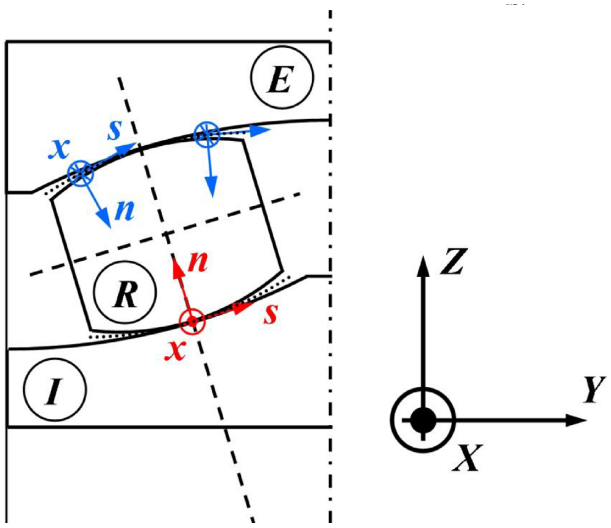


**Figure 4:** Potential contact surfaces and local contact coordinate systems in roller–raceway contacts of the spherical roller bearing.

## 3.2. Exact contact theory

In this work, a previously presented implementation of the exact contact theory named CECT (Blanco-Lorenzo *et al.*, 2016, 2018) is used, with the capability to solve conformal contact problems in non-planar contact surfaces. In the cited works, the application of CECT to wheel–rail contact problems was demonstrated. Here, its application to contact problems in rolling bearings is shown, and particular features of the implementation necessary for this application are described.

In the type of contact mechanics problems treated here, the CEM allows the construction of models with much fewer degrees of freedom than the FEM described in Section 3.3 for a similar level of detail in the contact solution. Further advantages of the exact contact theory are the use of a Eulerian mesh, by which the mesh is restricted to a region only slightly larger than the contact patch itself, and that it is possible to solve steady rolling contact problems directly, as opposed to the incremental or multistepping technique followed with the FE models described in Section 3.3. All this translates into much lower computational demands than the FEM simulation methodology used in this work.

A starting point of the contact analysis is the definition of the geometry of the potential contact surface, in which the contact patch of the rolling element with each raceway is contained. This is defined as a prismatic surface extruded along the *X* direction. Its profile is between the profiles of the rolling element and the raceway. Each contact is analysed in a local curvilinear {*x*, *s*, *n*} system associated with the potential contact surface. It moves with the contact patch, and its origin is defined to be in the corresponding nominal contact point. The *s* and *n* axes, of variable direction, are contained in the radial YZ plane. The *s* axis is tangent to the profile of the contact surface, and the *n* axis is normal to it, pointing into the rolling element. The *x* axis is perpendicular to the radial YZ plane, pointing towards the direction of the relative movement of the rolling element with respect to each raceway. Figure 4 depicts the {*x*, *s*, *n*} systems for the inner and outer contacts in different lateral positions. The profiles of the potential contact surfaces are also represented, in dotted lines. The *X* and *Y* axes of the {*X*, *Y*, *Z*} system are flipped for the analysis of each contact so that the *X* and *x* axes point in the same direction, to facilitate transformations between both systems.

The inner and outer contact problems are specified and solved independently, considering the relative motion of the rolling element with respect to each raceway. A Newton–Raphson iteration procedure is carried out to obtain the position, orientation, and rotation velocities of the rolling element with which its steady rolling equilibrium is satisfied. The main steps of the process are illustrated in the flowchart of Fig. 5.

In the steady equilibrium configuration, the sum of all the forces and moments acting on the rolling element, including the inertia forces, is zero, while the rolling element is in a steady configuration in the radial YZ plane. The rolling element configuration is defined with the following variables, which are arranged in a vector **{P}**:

1. Position, defined by displacements $d_Y$ and $d_Z$ of the rolling element centre in the YZ plane with respect to its nominal position.
2. Orientation, defined by rolling element tilt and skew angles $\beta$ and $\gamma$.
3. Rotation velocities $\omega_m$ and $\omega_R$.

A centrifugal force and gyroscopic moment are considered as inertia forces on the rolling element, with the magnitudes indicated in Section 2. An additional resultant force and moment may be considered acting on the rolling element, due for example to contact with the cage or lubricant churning. Here, these have been fixed at zero. The resultant forces and moments due to the contact, inertia, and additional forces and moments acting on the roller are summed in a vector **{R}**.

The main steps of the process illustrated in Fig. 5 for the determination of the steady equilibrium configuration of the roller are as follows:

1. **{P}** is initialized. This may be done with the nominal roller position or with a previously obtained equilibrium solution for a similar problem if one is available.
2. The inner and outer roller–raceway contacts are solved with CECT for the roller configuration defined in **{P}**.
3. **{R}** is calculated considering the previously obtained contact solutions. **{R}** is composed of subvectors $\mathbf{\{R_F\}}$ and $\mathbf{\{R_M\}}$ of forces and moments, respectively, each of them of three elements.
4. The condition for steady equilibrium is **{R}** = **{0}**. To check this condition, different tolerances are defined for $\mathbf{\{R_F\}}$ and $\mathbf{\{R_M\}}$, namely $tol_F$ and $tol_M$. If all the elements of $\mathbf{\{R_F\}}$ and $\mathbf{\{R_M\}}$ are below their respective tolerance (in absolute value), the equilibrium configuration of the roller has been found. Otherwise, a different **{P}** is tried. **{P}** is updated according to a Newton–Raphson algorithm as defined in the following steps.
5. **[J]** is calculated, the 6 × 6 Jacobian matrix that contains the sensitivities of each element of **{R}** to each element of **{P}**. This involves the solution of six pairs of inner and outer roller–raceway contact problems with CECT, one for each element of **{P}**, $P_i$. Each of these pairs of contact problems is solved considering a modified $\mathbf{\{P'_i\}}$ vector, in which $P_i$ is given a small increment $\delta P_i$ (i.e., $P_i$ is substituted by $P_i + \delta P_i$), and the rest of the elements are the same as in **{P}**. With each of these pairs of contact solutions, a modified resultant is obtained on the roller, $\{\mathbf{R'}_i\}$. The column of **[J]** corresponding to $P_i$ is calculated as $\partial\mathbf{\{R\}}/\partial P_i \approx (\{\mathbf{R'}_i\} - \mathbf{\{R\}})/\delta P_i$.
6. **{P}** is updated as $\mathbf{\{P\}}^{(n+1)} = \mathbf{\{P\}}^{(n)} - (\mathbf{[J]}^{-1})^{(n)}\ \mathbf{\{R\}}^{(n)}$. The superindices in parentheses $(n)$ and $(n+1)$ denote the iteration number.

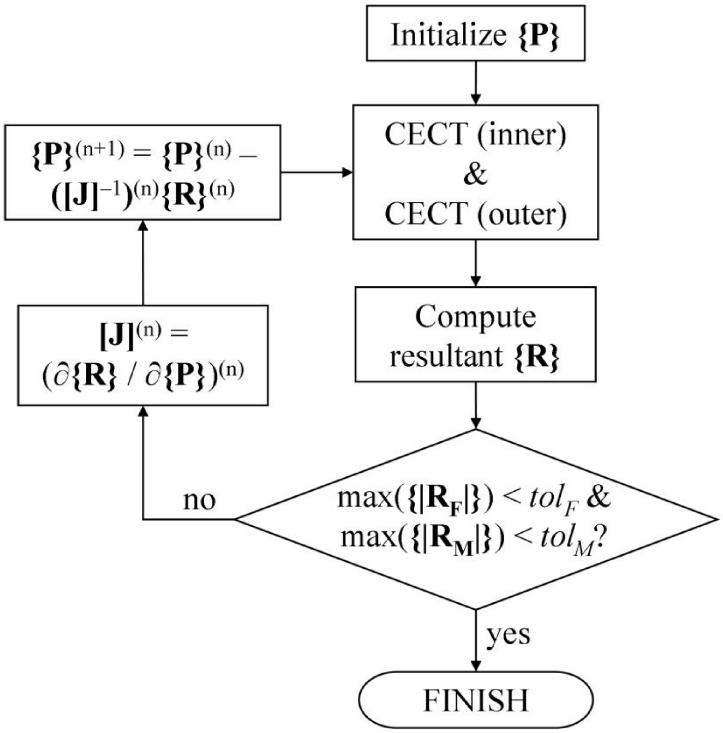


**Figure 5:** Flowchart of the search for the steady equilibrium configuration of the roller with contact solutions from CECT.

7. With the updated **{P}**, the process returns to step 2. Steps 2–6 are looped until **{R}** is sufficiently close to **{0}**, as defined by the tolerances $tol_F$ and $tol_M$.

The contact problems in step 2 above are solved with meshes of roughly 50 × 50 elements. Coarser meshes may be used in step 5 to save computation time. The matrix **[J]** presents a significant noise level due to discretization error when some element of the contact mesh changes from inside to outside contact or vice versa in some of the contact solutions computed in this step. This poses a considerable difficulty for the convergence of the Newton–Raphson process described earlier, and in some cases leads to divergence. This problem has been tackled by using very small increments $\delta P_i$, to avoid changes in the set of elements making up the contact patch. However, excessively small $\delta P_i$ increments could lead to being left with too few significant digits when computing the differences ($\{\mathbf{R}'_i\} - \{\mathbf{R}\}$), so some testing is necessary to arrive at adequate $\delta P_i$ values for the described numerical computation of **[J]**.

The application of the exact contact theory to rolling bearings is affected by the following two fundamental geometric differences between rolling element–raceway and wheel–rail contact:

1. The raceway is not straight in the rolling direction.
2. The rolling radii of the contacting surfaces of the rolling element and raceway are not large with respect to their variations in the contact patch.

Each of these points is addressed in the following subsections.

### 3.2.1. *Curvature of the raceway in the rolling direction*

The raceways are taken as bodies of revolution, like the rolling element. The axes of revolution of each pair of contacting bodies (inner raceway–roller and outer raceway–roller) may not be aligned nor contained in the same plane. The axis of revolution of the raceway is arranged to be aligned with the *Y* axis in each contact.

The inner raceway–rolling element contact is counterformal in the rolling direction. Additionally, the longitudinal curvature radii of the outer raceway are considered to be much higher than those of the rolling element. Within linear elasticity, this implies that the longitudinal dimensions of the contact patches are much smaller than these radii. So, the hypothesis of a prismatic contact surface previously described is retained for both the inner and outer contacts.

On the other hand, the longitudinal curvatures of the raceways affect the rolling element–raceway normal undeformed distances. The longitudinal dimension of the inner contact patch decreases as a result of the convex longitudinal curvature of the inner raceway, and that of the outer contact patch increases as a result of the concave longitudinal curvature of the outer raceway. The normal undeformed distances are computed following mostly the same procedure explained in Blanco-Lorenzo *et al.* (2016), which is based on computing intersections of the contacting surfaces with planes perpendicular to x. Only the computation of the intersections of the raceway surface is changed.

The intersections of the rolling element surface are computed in the same way as in the wheel–rail case, following a modification of the development to compute the wheel contact locus explained in appendix D of Li (2002). The key in this development is that the distance between the intersection of the wheel axis from the normal to the possible contact point on the wheel surface, to the centre of the rolling circle of that possible contact point, is known. Additionally, the possible contact point is in the same longitudinal position as the intersection mentioned earlier. Therefore, the longitudinal distance from the possible contact point to the centre of its rolling circle is known. Replacing in this development this distance by the distance to the plane perpendicular to x with which the intersection of the wheel surface is to be computed, expres-

sions for the exact coordinates of this intersection are obtained [cf. equations (11) and (12) of Blanco-Lorenzo *et al.* (2016)].

The intersections of the raceway surface are no longer constant in the *x* direction as with a straight rail. These are computed with the same equations as for the rolling element, particularized for having the raceway axis of revolution parallel to the *Y* axis. In this way, the *Z* coordinates of the raceway surface intersection are calculated as $\mathrm{sgn}(r_{\mathrm{roll},j}) \times \sqrt{r_{\mathrm{roll},j}^2 - \mathrm{x}^2}$, with $j \in \{I, E\}$. In this expression, $\mathrm{sgn}(r_{\mathrm{roll},j}) = 1$ if the raceway axis of revolution is below the point (x, s) = (0, 0) of the contact patch along the *Z* axis, and −1 otherwise. The raceway axis of revolution is defined to be at x = 0, and the origin of the *Z* coordinate is on this axis. The *Y* coordinates of the intersection are the same as those of the raceway profile on the *YZ* plane.

The longitudinal curvature of the raceway also implies that in steady rolling, the rotation velocity vector of the rolling element in its relative motion with respect to the raceway *j*, $\boldsymbol{\omega}_{\mathbf{R/j}}$, is not aligned with the axis of revolution of the rolling element *v*, unless *v* is parallel to the bearing *Y* axis. This is because $\boldsymbol{\omega}_{\mathbf{R/j}}$ is the vectorial sum of $\omega_{m/j}$ and $\omega_{\mathrm{R}}$. The rigid slip velocities are computed as the projections of the relative velocity vectors over the potential contact surface, following the same approach outlined in Blanco-Lorenzo *et al.* (2016). For this purpose, a new coordinate system {*u*′, *v*′, *w*′} is used, with the *v*′ axis parallel to $\boldsymbol{\omega}_{\mathbf{R/j}}$. The input data in this calculation are as follows:

1. $\boldsymbol{\omega}_{\mathbf{R/j}}$, with components $\omega_{\mathrm{R}/j,X}$, $\omega_{\mathrm{R}/j,Y}$, and $\omega_{\mathrm{R}/j,Z}$ in the {X, Y, Z} system.
2. $\mathbf{v}_{\mathbf{P/j}}$, the velocity vector of a point *P* on the rolling element relative to the raceway *j*, as well as the position of that point. $\mathbf{v}_{\mathbf{P/j}}$ has components $v_{P/j,X}$, $v_{P/j,Y}$ and $v_{P/j,Z}$ in the {X, Y, Z} system.
3. The mesh points of the potential contact surface on which the rigid slip velocities are to be computed. The vector from point *P* to an element *I* in the potential contact surface is $\mathbf{r}_{\mathbf{I\text{-}P}}$.
4. The angles of inclination *δ* of the potential contact surface in the *YZ* plane. The angle at element *I* is $\delta_I$. These angles are measured from the *Y* axis to the tangent to the potential contact surface directed in the positive *s* direction, counter clockwise as viewed looking towards the negative *X* direction. As the potential contact surface is prismatic, the angles *δ* vary only in the *s* direction.

Angles $\psi_\omega$ and $\varphi_\omega$ are computed according to equations (12) and (13).

$$\psi_\omega = \mathrm{atan}\left(-\omega_{\mathrm{R}/j,X}/\omega_{\mathrm{R}/j,Y}\right) \tag{12}$$

$$\varphi_\omega = \mathrm{sgn}\left(\boldsymbol{\omega}_{\mathrm{R}/j,Z}\right) \times \mathrm{acos}\left(\mathrm{sgn}\left(\boldsymbol{\omega}_{\mathrm{R}/j,Y}\right) \frac{\sqrt{\boldsymbol{\omega}_{\mathrm{R}/j,X}^2 + \boldsymbol{\omega}_{\mathrm{R}/j,Y}^2}}{||\boldsymbol{\omega}_{\mathbf{R/j}}||}\right) \tag{13}$$

The coordinate system {*u*′, *v*′, *w*′} is obtained from the system {*X*, *Y*, *Z*} with the following steps:

1. Rotation of $\psi_\omega$ around the *Z* axis. After this rotation, the orientation of the *u*′ axis, which is obtained from the *X* axis, is already defined.
2. Rotation of $\varphi_\omega$ around the *u*′ axis.
3. The origin of the system {*u*′, *v*′, *w*′} is translated to the point *P* on which the velocity $\mathbf{v}_{\mathbf{P/j}}$ is given.

The rigid slip velocity $\mathbf{w}_{\mathbf{I/j}}$ at an element *I* in the potential contact surface with respect to the raceway *j* is calculated by applying $\mathbf{w}_{\mathbf{I/j}} = \mathbf{v}_{\mathbf{P/j}} + \boldsymbol{\omega}_{\mathbf{R/j}} \times \mathbf{r}_{\mathbf{I\text{-}P}}$. Finally, $\mathbf{w}_{\mathbf{I/j}}$ is projected on the potential contact surface, and the rigid slip velocities $w_{I/j,x}$ and $w_{I/j,s}$ which are input in the tangential contact problem are obtained as the components of this projection on the principal directions of the surface *x* and *s*. The following expressions result:

$$\begin{aligned} w_{I/j,x} = {} & v_{P/j,X} + ||\boldsymbol{\omega}_{\mathbf{R/j}}|| \, R_I(-\cos(\theta_I)\cos(\psi_\omega) \\ & + \sin(\theta_I)\sin(\psi_\omega)\sin(\varphi_\omega)) \end{aligned} \tag{14}$$

$$\begin{aligned} w_{I/j,s} = {} & v_{P/j,Y}\cos(\delta_I) + v_{P/j,Z}\sin(\delta_I) + ||\boldsymbol{\omega}_{\mathbf{R/j}}|| \, R_I \\ & \times (-\cos(\delta_I)\cos(\theta_I)\sin(\psi_\omega) \\ & - \cos(\delta_I)\sin(\theta_I)\cos(\psi_\omega)\sin(\varphi_\omega) \\ & + \sin(\delta_I)\sin(\theta_I)\cos(\varphi_\omega)) \end{aligned} \tag{15}$$

In equations (14) and (15) $R_I$ and $\theta_I$ are, respectively, the radial and azimuthal coordinates of the vector $\mathbf{r}_{\mathbf{I\text{-}P}}$ in a cylindrical coordinate system with its axial direction aligned with the *v*′ axis and having the origin of the *θ* coordinate on the negative *w*′ axis.

### 3.2.2. *Varying rolling radii of the contacting surfaces*

The following relation of velocities holds in the tangential contact problem:

$$\mathbf{v} = \mathbf{w} + \frac{\mathrm{D}\mathbf{u}}{\mathrm{D}t} = \mathbf{w} + V_c \frac{\partial \mathbf{u}}{\partial x} + \frac{\partial \mathbf{u}}{\partial t} \tag{16}$$

In equation (16), $\mathbf{v}$ is the slip velocity, $\mathbf{w}$ is the rigid slip velocity, and $\mathbf{u}$ is the tangential elastic displacement difference of the contacting surfaces. They are 2D vectors with components in the (*x*, *s*) tangent directions of the contact surface. These vectors are functions of the (*x*, *s*) surface position in the contact reference frame and in non-stationary problems of time as well. The uppercase time derivative on the central side of the equation denotes a Lagrangian derivation associated with the material particles of the contacting surfaces. $V_c$ is the rolling or contact velocity, approximately the velocity at which the material particles of the bodies flow through the Eulerian {*x*, *s*, *n*} coordinate system attached to the contact patch along the negative *x* direction, or in other words, the velocity of the contact over the contacting surfaces in the relative motion with respect to each contacting surface. In wheel–rail contact, $V_c$ may be taken as uniform throughout the whole contact. In rolling bearings, it may be variable because the rolling radii of the bodies may be variable. This affects the computation of the surface velocities associated with the elastic deformations of the contact surfaces, i.e., the second term on the central side of equation (16).

The discretization in time of equation (16) leads to

$$\mathbf{v} = \mathbf{w} + \frac{\mathbf{u} - \mathbf{u}'}{\Delta t}. \tag{17}$$

In equation (17), $\Delta t$ is the chosen increment for the time discretization, $\mathbf{u}$, $\mathbf{v}$, and $\mathbf{w}$ are field magnitudes in the current time instant *t*, and $\mathbf{u}'$ is the elastic displacement difference in the previous time instant and position. For the contacting particles occupying position (x, s) in the current time instant *t*, $\mathbf{u}' = \mathbf{u}'(x, s, t) = \mathbf{u}(x + V_c\,\Delta t, s, t - \Delta t)$. The quantity $V_c\,\Delta t$ is designated as $\Delta q$. $\Delta t$ is fixed for the whole contact patch, so with a variable $V_c$, $\Delta q$ is variable in the contact patch. A reference $\Delta q$, $\Delta q_o$, is chosen in the contact patch. This may be the value of $\Delta q$ at (x, s) = (0, 0), for example. $\mathbf{u}'$ is obtained in different ways in transient and in steady-state rolling contact problems.

In transient rolling contact problems, the elastic displacement field in the previous time instant is known. It is computed with the contact stresses of the previous time instant, $\mathbf{p}' = \mathbf{p}(x, s, t - \Delta t)$, according to equation (18).

$$\mathbf{u'}_{\mathbf{Ii}} = [\mathbf{IC'}_{\mathbf{IiJj}}]\mathbf{p'}_{\mathbf{Jj}} \tag{18}$$

Equation (18) expresses the discretized relationship between contact surface stresses and elastic displacements at $t - \Delta t$. A similar relationship may be written for the current time $t$. $\mathbf{p'_{Jj}}$ is the vector of contact stresses at time $t - \Delta t$, with element $p'_{Jj}$ of this vector being the contact stress along direction $j \in \{x, s, n\}$ on element $J$ of the contact mesh. The index $J$ is extended over all the elements of the mesh entering into contact. $\mathbf{[IC'_{IiJj}]}$ is a matrix of ICs of the contact mesh. Element $IC'_{IiJj}$ of this matrix gives the elastic displacement difference along direction $i \in \{x, s\}$ on element $I$ due to a unit stress along direction $j$ on element $J$, at the position $(x_I + \Delta q_o, s_I)$ occupied by the particles of element $I$ in a previous instant. Different alternatives for the efficient approximation of the ICs of solids with non-planar surfaces are proposed in Blanco-Lorenzo *et al.* (2021). In this work, the approximation designated as $\hat{B}$ in that reference is used. Here, it is generally desirable a common $\Delta q_o$ for the whole contact mesh for efficiency in the computation of ICs and their convolution(With a regular mesh, the convolution of the ICs with the contact stresses may be performed efficiently in the Fourier domain with FFTs, and without forming complete $NE \times NE$ $\mathbf{[IC'_{IiJj}]}$ matrices for a 2D mesh with $NE$ elements, as explained e.g., in Liu *et al.* (2000). This, however, is not relevant to the subject discussed here, and the variables and equations in this section are expressed in the space domain for convenience. In planar contact problems, the surface displacements may be obtained with a 2D convolution applying 2D FFTs. In non-planar contacts, generally, the similarities between ICs in the lateral direction are lost, and full 2D convolutions are no longer possible. In this case, the surface displacements of each lateral position of the mesh may be computed as the sum of $n_s$ 1D convolutions in the longitudinal direction applying 1D FFTs ($n_s$ being the number of divisions of the mesh in the lateral direction)) with the contact stresses. To get the desired displacements at $(x_I + \Delta q, s_I, t - \Delta t)$, the initially obtained displacements at $(x_I + \Delta q_o, s_I, t - \Delta t)$ are interpolated in the $x$ direction (or extrapolated as necessary at extreme positions of the mesh).

In steady rolling contact problems, the transient term $\partial\mathbf{u}/\partial t$ on the right-hand side of equation (16) vanishes, and the second term on the right-hand side of equation (17) becomes a purely spatial gradient. Therefore, the difference $\mathbf{u} - \mathbf{u'}$ in this term may be scaled proportionally to $V_c$ in each mesh position.

$(\mathbf{u} - \mathbf{u'})$ is split into the contributions due to the normal pressures and the tangential tractions, $(\mathbf{u} - \mathbf{u'})_n$ and $(\mathbf{u} - \mathbf{u'})_t$, with $(\mathbf{u} - \mathbf{u'}) = (\mathbf{u} - \mathbf{u'})_n + (\mathbf{u} - \mathbf{u'})_t$. Following the Panagiotopoulos process to solve the generally coupled normal–tangential contact problem (Panagiotopoulos, 1975; Kalker, 1990), $(\mathbf{u} - \mathbf{u'})_t$ is initially unknown, and $(\mathbf{u} - \mathbf{u'})_n$ is known in the tangential problem. If the available $(\mathbf{u} - \mathbf{u'})_n$ corresponds to a common $\Delta q_o$ in the whole contact patch, the value for the applicable $\Delta q$ in each position is obtained by scaling $(\mathbf{u} - \mathbf{u'})_n$ with the ratio $\Delta q/\Delta q_o$.

For $(\mathbf{u} - \mathbf{u'})_t$, this scaling is realized by modifying the elements of the matrices of ICs with which this difference is computed within the solver used for the tangential problem. This may be calculated according to equation (19) or to equation (20). The **[IC]** matrix in these equations is homologous to the previously explained **[IC']** matrix for the current time instant $t$. In either case, the fact that in steady rolling $\mathbf{p'} = \mathbf{p}(x, s, t)$ is used. The subindices $IiJj$ used in equation (18) are dropped in these equations for brevity, and here $j \in \{x, s\}$.

$$(\mathbf{u} - \mathbf{u'})_t = ([\mathbf{IC}] - [\mathbf{IC'}])\,\mathbf{p} = [\mathbf{dIC}]\mathbf{p} \tag{19}$$

$$(\mathbf{u} - \mathbf{u'})_t = [\mathbf{IC}]\,(\mathbf{p}\,(x, s, t) - \mathbf{p}\,(x + \Delta x, s, t)) = [\mathbf{IC}]\mathbf{dp} \tag{20}$$

Referring to equation (19), if the initially computed difference matrix **[dIC]** corresponds to a common $\Delta q_o$ in the whole contact patch (i.e., if **[dIC]** = **[dIC**$(\Delta q_o)$**]**), a scaled difference matrix $\mathbf{[dIC_{sc}}(\Delta q)\mathbf{]}$ is used within the tangential solver instead of **[dIC**$(\Delta q_o)$**]**. Each element of $\mathbf{[dIC_{sc}}(\Delta q)\mathbf{]}$ is computed as $dIC_{sc,IiJj}(\Delta q) = dIC_{IiJj}(\Delta q_o) \times \Delta q_I/\Delta q_o$, being $\Delta q_I$ the value of $\Delta q$ at the position of element $I$. Regarding equation (20), which is used in the SteadyGS tangential solver (Vollebregt, 2010), $\Delta x$ is the element size in the longitudinal direction, common in the whole contact mesh. In this case, the scaling of **[IC]** is performed analogously as explained for **[dIC]** in equation (19). In either case, it has to be borne in mind that this scaling is valid only for computing differences $(\mathbf{u} - \mathbf{u'})_t$, but not values $\mathbf{u}$ or $\mathbf{u'}$. Equations (19) and (20) become

$$(\mathbf{u} - \mathbf{u'})_t = [\mathbf{dIC_{sc}}\,(\Delta q)]\mathbf{p} \tag{21}$$

$$(\mathbf{u} - \mathbf{u'})_t = [\mathbf{IC_{sc}}\,(\Delta q)]\mathbf{dp}. \tag{22}$$

The calculation of $V_c$ is carried out in a similar way as described in Section 3.1, using equations (5) and (6) to compute contact velocities $V_{c,j}$ and $V_{c,R}$ over the surfaces of the raceway and rolling element. The contact velocities may be approximated as constant in $x$ in this calculation due to the short longitudinal dimension of the contact patch. $V_c$ and $\Delta q$ may therefore be taken as variable only in the $s$ direction. For the general case of contacting bodies with dissimilar elastic constants, $V_c$ is computed as the weighted average of $V_{c,j}$ and $V_{c,R}$, using the elastic constant $E_B{}^* = E_B/(1 - \nu_B{}^2)$ of each body $B$ as weight. A possible refinement could be to retain the velocities $V_{c,j}$ and $V_{c,R}$ to compute the velocities due to elastic deformations of each surface separately instead of using a single, averaged $V_c$. This would require doubling the amount of IC matrices to be handled. However, if the difference between these velocities is not small, there will be large rigid slip velocities, which in linear elasticity will dominate the resultant slip velocities $\mathbf{v}$ as Kalker pointed out (Kalker, 1990, 2001). In this case, a slight improvement in the computation of the term $(\mathbf{u} - \mathbf{u'})/\Delta t$ of equation (17) is not relevant.

In the considered spherical roller bearing, it has been observed that using a variable contact velocity across the contact patch to compute the velocities $(\mathbf{u} - \mathbf{u'})/\Delta t$ has little influence on the tangential problem solution, because the variations of the rolling radii are relatively modest and because there are large rigid slip velocities in most of the contact patch as a result of the curved profiles of the roller and the raceways. However, having a curved raceway in the rolling direction makes possible to have significant variations in the rolling radii across the contact patch without having large rigid slip velocities. For example, in the case of steep-angle tapered roller bearings, this effect may be more relevant.

### 3.3. FEM

The FE model for the calculation of the roller–raceway contacts comprises one roller and a portion of the inner and outer rings in contact with it. It has been built in Abaqus/Standard (Dassault Systèmes Simulia Corp., 2012). A general view of the model is shown in Fig. 6a. The contact regions of the roller and the raceways are finely meshed with solid linear hexahedron C3D8 elements. Figure 6b shows a detail of the mesh of the roller surface in the most finely meshed region. The minimum element size is approx. 0.024 × 0.37 × 0.06 mm (in longitudinal, lateral, and depth directions, respectively). The model has a total of about 740 000 nodes. Frictional contact pairs are defined between the rolling surfaces of the roller and the inner and outer raceways. A surface-to-surface contact detection method is used, and the contact con-

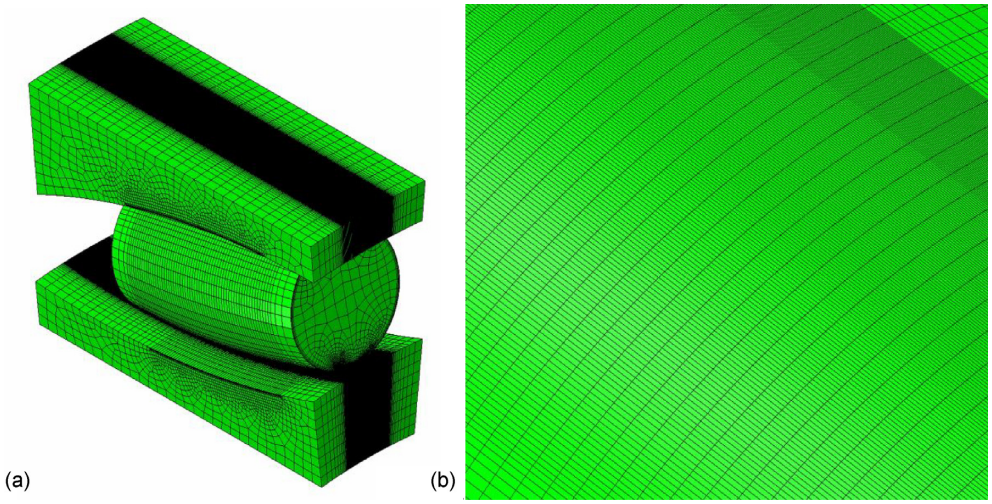


**Figure 6:** 3D FE model for contact analysis of spherical roller bearing. (a) General view. (b) Mesh detail.

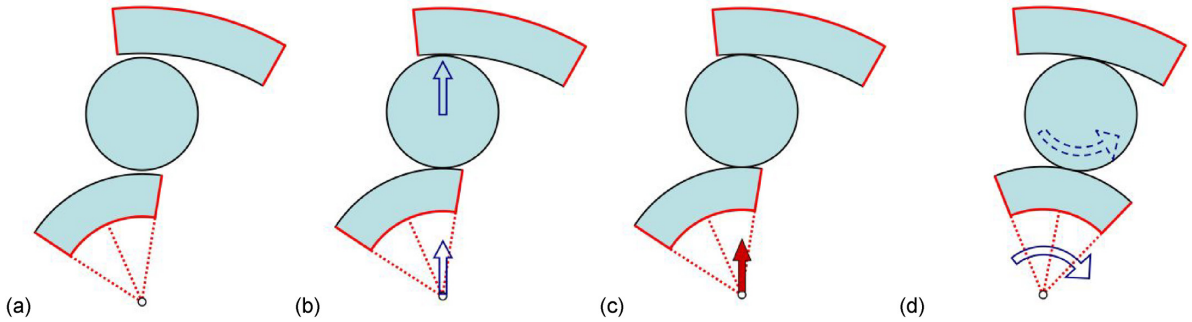


**Figure 7:** Main phases of the FEM rolling contact simulations of the spherical roller bearing. (a) Initial position. (b) Initial approach. (c) Normal load. (d) Rolling.

straints are enforced with the penalty method, both for the normal and tangential parts.

The rolling contact between the roller and the inner and outer rings is simulated in a Lagrangian, multistep static simulation. A central reference node is defined for each ring, through which their motion is prescribed. The main phases of the FEM simulation are the initial positioning and normal loading of the roller and the rolling stage. These are illustrated in Fig. 7. The figure shows a schematic view of the two rings and the roller perpendicular to the bearing Y axis during the different simulation phases. The central node of the outer ring is fully constrained during the whole simulation.

All the bodies are initially positioned in such a way that the inner and outer contacts fall into the most finely meshed regions of the contact surfaces at the end of the simulation. The axial position of the roller also has to be adjusted at the beginning of the simulation, as explained in Section 4.2.

The normal loading phase is split into two steps, depicted in Fig. 7b and c. In the first of these steps, small radial displacements are imposed on the roller and inner ring to achieve the initial closure of the inner and outer contacts. This is indicated by the blue vertical arrows on the central points of the inner ring and the roller. This displacement-controlled step is necessary because before achieving the initial contact closure the system is singular if the rigid body motion of the bodies is not constrained. In the second step of the normal loading phase (Fig. 7c), the radial displacement constraints of the roller and the inner ring are released, and the desired radial load is imposed on the central node of the inner ring. This is indicated by the red vertical arrow on the central point of the inner ring. At the end of this step, the roller is in equilibrium under the inner and outer contact forces and the inertia forces applied through the central node of the roller as prescribed concentrated forces and moments. The resulting normal approach of this node towards the outer ring at the end of this phase is held constant during the subsequent rolling stage.

During the rolling stage (Fig. 7d), small axial rotation increments are imposed on the central node of the inner ring. Thus, the motions of the central nodes of the rings are entirely prescribed, while the movement of the roller is driven by the contacts with the inner and outer raceways. The rolling phase of the simulation is also split into several steps. The applied axial rotation increments to the inner ring are adjusted according to the mesh density of the surface sections traversed by the contact patches in each of these steps for the displacement increments of the contact patches in each substep to be similar to the mesh element size in the longitudinal direction.

A quasi-stationary rolling contact state is established at the contact level within rolling distances of the order of a few times the longitudinal contact patch dimension [1–2 times as shown by experience with the exact contact theory, as quoted in Kalker (1979)]. On the other hand, in the simulations carried out, it has been observed that larger rolling distances are required for the roller to reach a steady configuration, as is shown in Section 4.2. Simulations with inner ring rotated angles of up to 170 mrad

have been carried out in this work, which corresponds to a roller–raceway rolled distance of about 7.6 mm, or about 17 times the total longitudinal dimension of the outer contact patch with a normal load of 5.5 kN between the roller and each raceway. In contrast, much lower rolled distances have been seen to be necessary in other applications of detailed FEM for rolling contact analyses in rolling bearings. For example, a rolled distance of one time the longitudinal contact patch dimension was applied in Heras *et al.* (2017b), observing that this was sufficient for the friction torque to stabilize.

Taking into account the large size of the model, which includes two finely meshed contact regions, and the long rolling distances, the mesh construction and simulation set-up have to be properly optimized to get affordable FEM simulations. With this aim, a variable mesh density has been used in the rolling direction, as may be appreciated in Fig. 6b, providing the finer mesh in the final part of the simulated rolling path in each contact surface. Compared to wheel–rail rolling contact FEM simulations shown in previous works (Blanco-Lorenzo *et al.*, 2016, 2018), these roller–raceway rolling contact simulations have presented greater difficulty. The fact of having the roller driven just by the contacts with the rings rather than with prescribed motion, as well as the increased model size, contributes to the added complexity.

## 4. Results

The partial slip contact models described in Section 3 have been used to compute roller–raceway frictional contact solutions for the spherical roller bearing described in Section 2. First, the performance of the considered contact models is assessed in Section 4.1. In Section 4.2, the quality of the contact solutions obtained with FEM is discussed, examining the evolution of relevant output quantities along the simulations. Lastly, Section 4.3 presents a study of the steady rolling equilibrium attitudes of the roller in a range of normal loads and friction levels.

### 4.1. Comparison of strip theory, CECT, and FEM

In this section, the roller–raceway contact solutions obtained with the contact models described in Section 3 are compared, to assess the ability of each model to produce representative results. For this purpose, the steady rolling positions of the roller with a normal load $N$ of 5.5 kN and two different values of the coefficient of friction $\mu$, namely $\mu = 0.10$ and 0.30, are considered. Besides comparing the results of the different models, the main features of the contact solutions are illustrated for different friction levels. With $\mu = 0.10$, most of the contact patch is sliding. With the higher $\mu$, a bigger adhesion zone is obtained, and the elasticity of the bodies plays a more important role in the tangential contact. A partial slip contact model may provide a greater precision improvement in the contact solutions in the latter case, with respect to a full slip contact model.

Two different solutions computed with strip theory are included in each case, labelled as 'H+C' (Hertz + Carter). The difference between both solutions is the position of the roller–raceway contact centres. In one of them, each roller–raceway contact centre is located in its nominal position. This is identified with '$s_0 = 0$'. In the other, identified with '$s_0 = s_{0\_CECT}$', the roller–raceway contact centres are offset from their nominal positions in the contact lateral (s) direction. The same offset is applied for the inner and outer contacts, computed as the average of the offsets for each contact of the corresponding equilibrium solution computed with CECT.

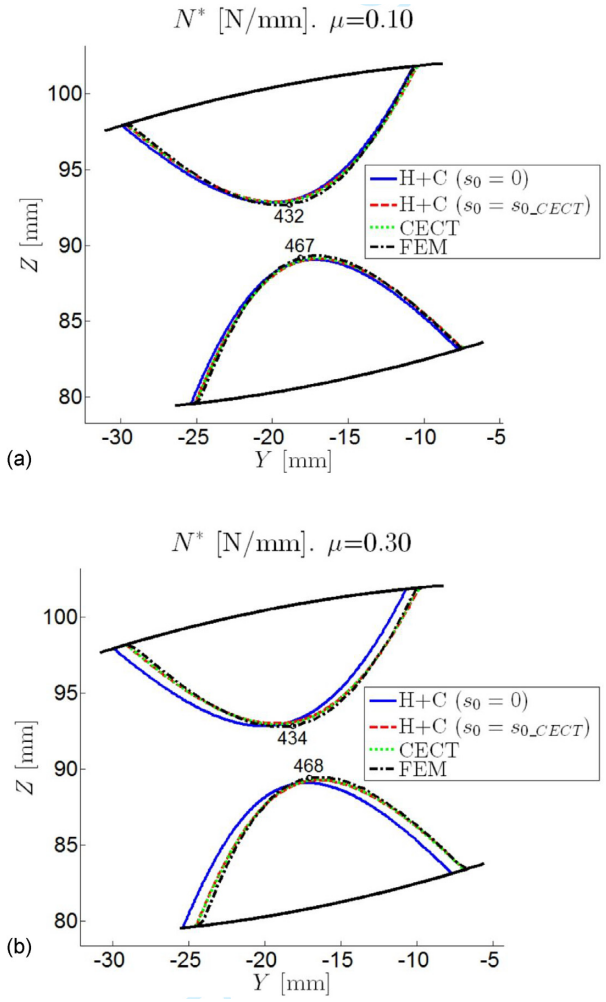


**Figure 8:** Lateral distribution of normal load in roller–raceway contacts with $N = 5.5$ kN. (a) $\mu = 0.10$. (b) $\mu = 0.30$.

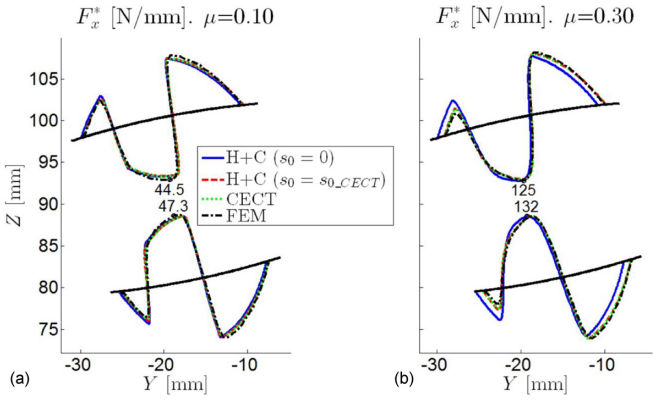


**Figure 9:** Lateral distribution of traction in roller–raceway contacts with $N = 5.5$ kN. (a) $\mu = 0.10$. (b) $\mu = 0.30$.

Figures 8 and 9 show the lateral distributions of normal load and longitudinal tractions per unit contact width, $N^*$ and $F_x^*$, across the inner and outer contact patches. The contact patches appear offset from their nominal position towards the positive y direction, as can be seen comparing the CECT and FEM solutions with the H+C ($s_0 = 0$) solution. This offset is higher for higher $\mu$. The reason for this offset is explained in Section 4.3. The FEM so-

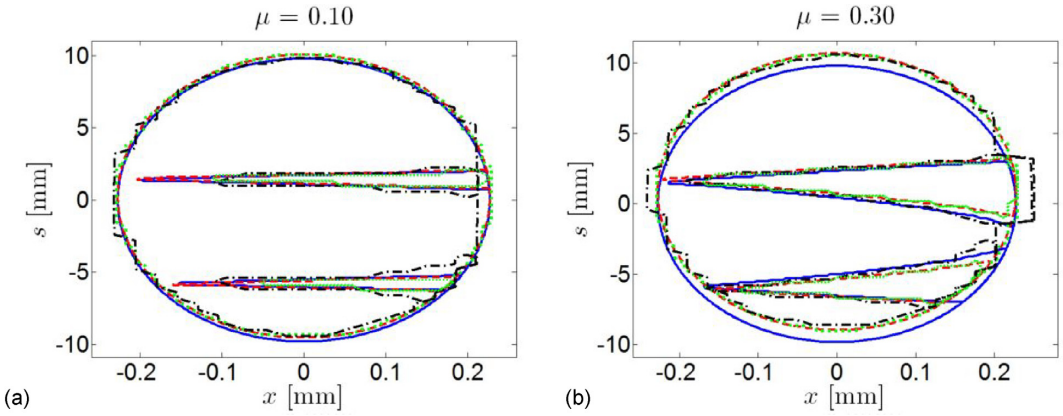


**Figure 10:** Contours of adhesion and slip zones in the outer roller–raceway contact patch with $N = 5.5$ kN. Solid blue: H+C ($s_0 = 0$); dashed red: H+C ($s_0 = s_{0\_CECT}$); dotted green: CECT; chain black: FEM. (a) $\mu = 0.10$. (b) $\mu = 0.30$.

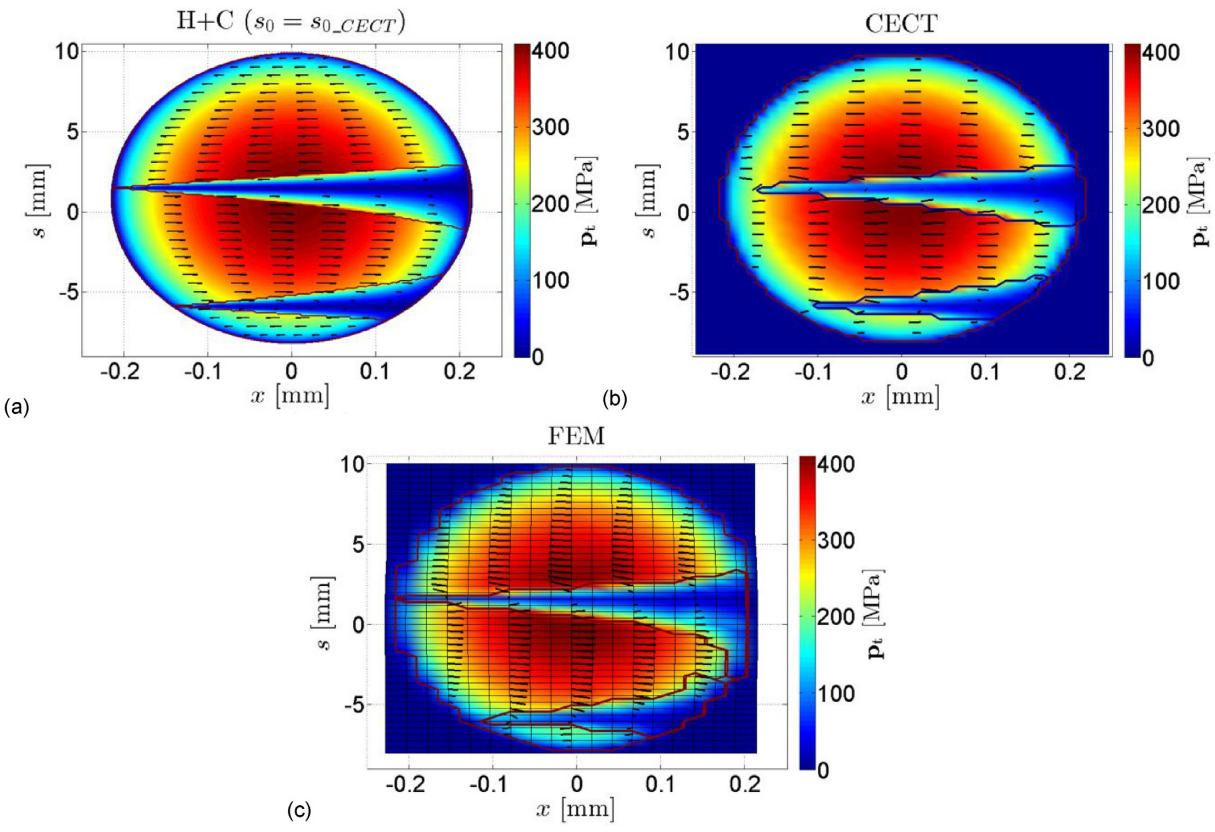


**Figure 11:** Magnitude and direction of tangential stresses and contours of adhesion and slip zones in inner roller–raceway contact patch with $N = 5.5$ kN and $\mu = 0.30$. (a) H+C ($s_0 = s_{0\_CECT}$). (b) CECT. (c) FEM.

lutions give a slightly more concentrated load distribution in the lateral direction, as seen in Fig. 8. Apart from this, there are no remarkable differences in the normal contact solutions obtained with H+C ($s_0 = s_{0\_CECT}$), CECT, and FEM.

Figures 10 and 11 show the contact patch contours and the tangential stresses. As is characteristic with crowned rollers, the tangential contact solutions are dominated by high longitudinal creepages due to the variable rolling radii of the roller across the contact with the raceways, with two zero-slip bands in which they change sign. This may also be seen in the longitudinal traction distributions of Fig. 9. A good match is observed between the different solutions in the tangential contact as well. On the other hand, mostly with high $\mu$ notable differences are seen between the H+C solutions obtained with and without adjusted contact centre positions. These differences may be clearly appreciated in the lateral distributions of frictional work shown in Fig. 12. This shows that not making the lateral contact position adjustment may lead to some inaccuracy in the tangential contact solution. While quite accurate results may be obtained with H+C, it is not possible to work out the necessary equilibrium condition in the lateral direction to perform this position adjustment taking into account only the longitudinal tangential stresses in the calculation. The differences between both H+C solutions are higher with higher $\mu$ because the roller shift between its equilib-

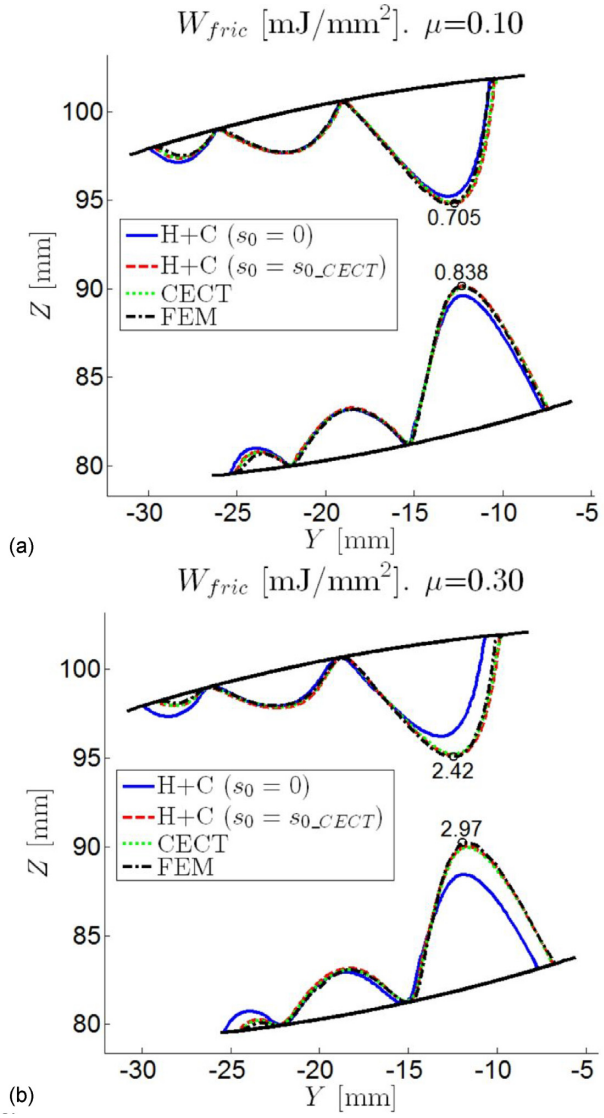


**Figure 12:** Lateral distribution of frictional work in the inner and outer races after one roller passage with $N = 5.5$ kN. (a) $\mu = 0.10$. (b) $\mu = 0.30$.

rium and nominal position increases for higher $\mu$, as explained in Section 4.3.

The slip velocities and frictional work levels are higher towards the bearing XZ centre plane, as can be seen in Fig. 12. Here, the longitudinal creepage due to the rolling radii difference of the roller surface with the rolling cone is superposed with the spin creepage. The lateral contact shift is produced towards this side, and consequently, the maximum frictional power densities in the contact patch increase.

Due to the short longitudinal dimension of the contact patches, the slip velocities are primarily aligned in the rolling direction, except around the zero-slip bands. Figure 13 shows longitudinal distributions of slip velocities along slices close to one of these regions. In the case with low $\mu$, notable differences are observed between the H+C, CECT, and FEM results around the zero-slip bands, where the tangential stresses change from their positive to their negative saturation bounds in a relatively small distance in the lateral direction. In this region, significant lateral components of stress and slip velocities appear, as seen in Fig. 13a, and the 2D simplification is inadequate. Part of the differences between the CECT and FEM results seen in Fig. 13a may be attributed to the fact that the lateral positions in which the results are taken in each model are not exactly the same. The results obtained with CECT and FEM indicate higher levels of tangential stresses and slip than predicted with the strip theory neglecting the interaction between adjacent strips. Nevertheless, these regions occupy a small part of the whole contact patch.

In the case with high $\mu$, the changes of $\xi^*$ are slower in the lateral direction, which implies lower interaction between adjacent strips. Consequently, the lateral components of stress and slip velocities are comparatively smaller, and a better agreement is found between the tangential stresses (not shown in the figure) and slip velocities obtained with H+C, CECT, and FEM, as shown in Fig. 13b. Figure 14 shows the distributions of longitudinal rigid slip in the outer contact, for $\mu = 0.10$ and 0.30, both in terms of longitudinal rigid slip velocities $w_x$ and normalized longitudinal creepages $\xi^*$. The graphs for the inner contact are qualitatively similar. While the profiles of $w_x$ are similar for both values of $\mu$, the profiles of $\xi^*$ are different mainly due to the different $\mu$. Here, it is also shown for each $\mu$ how $\xi^*$ changes as a result of the lateral shift of the contact, mainly for high $\mu$ where the shift is higher.

## 4.2. Assessment of stationarity of FEM solutions

Figure 15 shows the evolution along a FEM simulation of different parameters that are checked to determine whether the obtained FEM results correspond to stabilized equilibrium positions. The results shown correspond to the case of Section 4.1 with $\mu = 0.30$. Similar trends are observed for the case with $\mu = 0.10$, with some of the parameters stabilizing earlier.

Figure 15a shows the resultant tangential forces in each contact. The lateral tangential forces become reasonably stabilized within the first half of these simulations after a rolled distance of about eight times the longitudinal dimension of the contact patch (a rolled distance equal to the longitudinal dimension of the outer contact patch corresponds to a rotated angle of the inner ring $\theta_I$ of about 10 mrad, cf. Section 3.3). The longitudinal forces reach stabilization earlier.

Figure 15b shows the lateral locations of the centres of the normal pressures of the inner and outer contacts, $Y_{c,i}$ and $Y_{c,e}$. Their evolution is determined primarily by roller tilting in this simulation. The roller also has a slight lateral motion, also shown in these figures in non-dimensional form $\eta$ as the axial velocity of the roller centre $v_{R,y}$ divided by the rolling speed along the outer contact centreline. This does not represent exactly the lateral creepage in the roller–raceway contact, as it does not include the part due to roller skew.

The lateral motion of the roller causes variations in the contact lateral resultant forces enough to comply quasistatic equilibrium of the roller in significantly different lateral positions. The lateral position of the roller influences the lateral shift of the contact patches, which impacts on the tangential solution, as shown in Section 4.1. The actual steady equilibrium position of the roller is the one with zero $\eta$. Reaching this position from an arbitrary initial position would require impractically long rolling distances for this FE model. In this work, the correct equilibrium lateral position of the roller is found iterating with different initial lateral positions. In this way, plots of $\eta$ versus roller lateral position, such as the ones shown in Fig. 16, are produced. In this figure, $d_y$ designates the axial offset of the roller centre from its nominal position along the y axis. The changes of $d_y$ are of the order of just 1 micron in these simulations. This shows that an accurate analy-

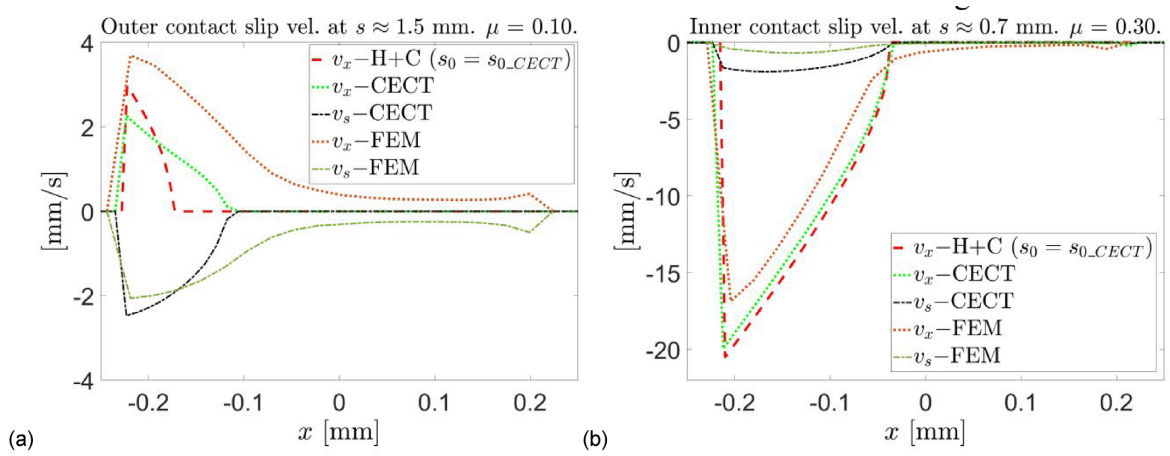


**Figure 13:** Longitudinal distribution of slip velocities at lateral positions of the roller–raceway contacts partly in adhesion. $N = 5.5$ kN. (a) $\mu = 0.10$. Outer contact—at $s = 1.54$ mm in H+C results, 1.52 mm in CECT results, and 1.60 mm in FEM results. (b) $\mu = 0.30$. Inner contact—at $s = 0.68$ mm in H+C and CECT results and 0.80 mm in FEM results.

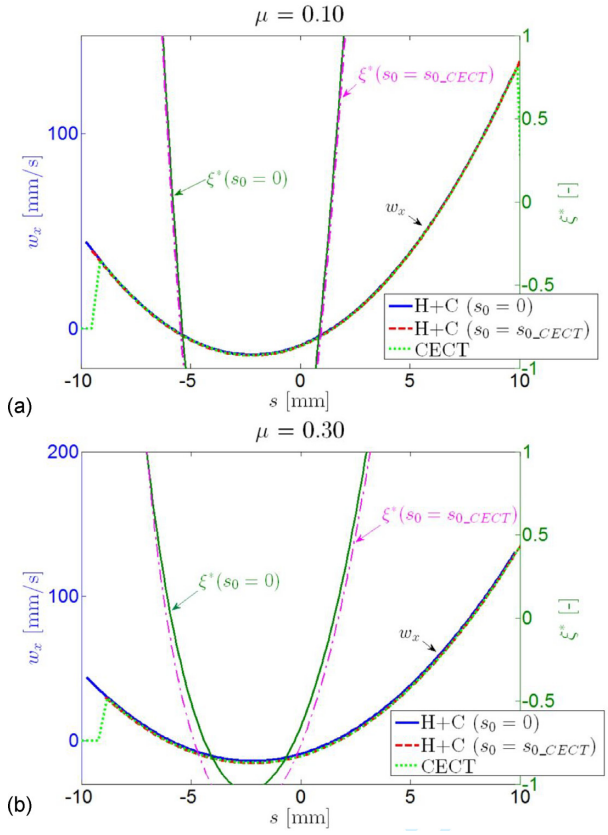


**Figure 14:** Lateral distribution of longitudinal rigid slip in the outer roller–raceway contact with $N = 5.5$ kN. (a) $\mu = 0.10$. (b) $\mu = 0.30$.

sis of the motions of the roller is necessary to interpret the FEM results correctly and to obtain the steady rolling solution. Given the slow lateral movement of the roller in lateral positions different from the one corresponding to steady equilibrium, the roller may not reach its steady-state equilibrium position during its whole orbiting motion around the bearing in some cases.

The trends of roller tilt and skew shown in Fig. 15c indicate that the tilt is stabilized during the simulation, but not the skew. Nevertheless, the skew angle variations are not very high, and the values obtained in the final phase of this simulation are close to the value computed with CECT for steady equilibrium, with a difference of just about 0.2 mrad. The differences in the tilt angles obtained with CECT and FEM are of the same order. It is considered that these angles are small enough to be able to take the FEM solution as a representative steady equilibrium solution.

Calculations with CECT indicate that the individual contact lateral resultant forces in the inner and outer contacts are relatively sensitive to the tilt and skew angles. Higher negative tilt and skew angles lead to higher lateral force in the outer contact and lower in the inner contact, and higher negative skew also leads to slightly higher total lateral force. Indeed, the individual lateral contact forces computed with CECT and FEM do not match well. However, other results, such as the total lateral resultant force on the roller from the inner and outer contacts, the roller axial displacement $d_y$, and the resultant longitudinal forces, are not so sensitive to these angles, and a relatively good agreement is found between the CECT and FEM results, as shown in Table 2 for the cases of Section 4.1. The table includes the longitudinal and lateral frictional forces in each contact, $F_x$ and $F_{lat}$, and the sum of the lateral forces in the inner and outer contacts $\sum F_{lat}$. All the forces are divided by $\mu N$.

Apart from the CECT and FEM results, Table 2 also shows the results of a full slip solution for each friction level. These full slip solutions have been derived from the CECT equilibrium solution for each case, considering the corresponding normal pressure distributions and rigid slip velocities computed with CECT, as follows. At each point of the contact patch, the magnitude of the tangential stress is defined as the normal pressure times the coefficient of friction, and its direction is determined with the direction of the rigid slip. The resultant contact forces are then obtained as the vector sum of the contributions of each element of the mesh of the contact surface, as in the other models. The full slip solutions obtained in this way are not equilibrium solutions; these would have to be computed for other roller (equilibrium) configurations through a procedure such as that shown in Fig. 5. It is observed that the lateral forces, and mostly the values of their sum $\sum f_{lat}$ for the full slip solutions, are much lower than the corresponding values obtained with CECT and with FEM. This was to be expected, as the lateral force due to spin (the camber thrust) is absent in symmetric contact patches with the full slip model. Consequently, the equilibrium configurations obtained with the

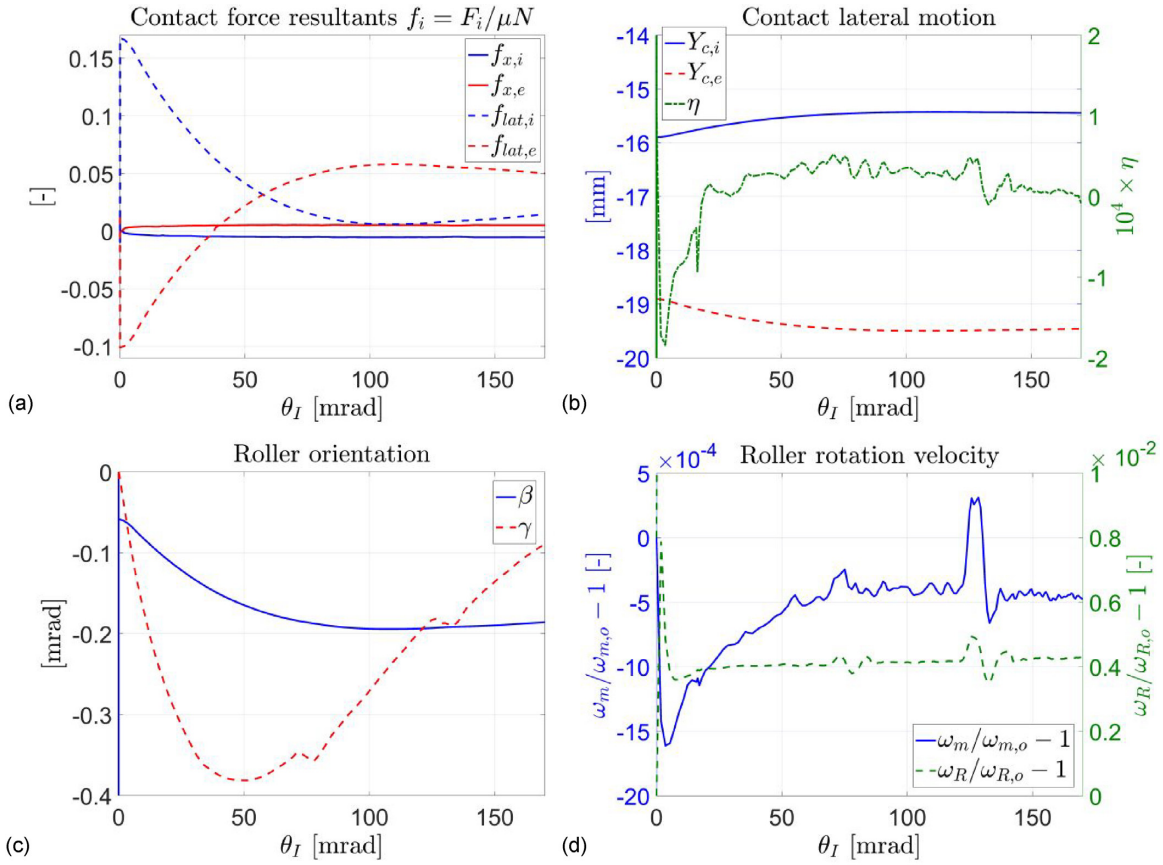


**Figure 15:** Indicators of stationarity of FE rolling contact solution for $N = 5.5$ kN and $\mu = 0.30$ along the rolling stage of simulation. (a) Frictional contact resultant forces $f_i = F_i/\mu N$. (b) Axial positions in bearing of centres of contact normal pressures, and lateral displacement of roller. (c) Roller orientation (tilt $\beta$ and skew $\gamma$). (d) Roller rotation velocities $\omega_m$ and $\omega_R$.

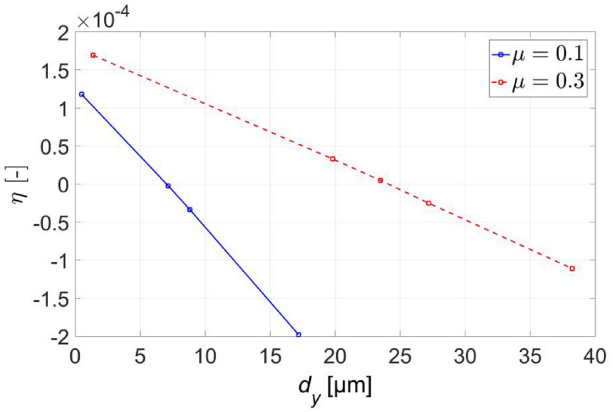


**Figure 16:** Non-dimensional axial velocity of roller $\eta$ as a function of its initial lateral position in FEM rolling contact simulations.

full slip solutions would surely have much lower $d_y$ displacements than the ones computed with CECT and FEM, cf. Section 4.3.

Figure 15d shows the trends of the rotation velocities $\omega_m$ and $\omega_R$ of the roller relative to their theoretical values corresponding to perfect rolling on the nominal contact points. It may be seen that the roller rotation velocities are also stabilized by the end of these simulations. The perturbations seen in the trends of these velocities, $\eta$ and $\gamma$ at about 75 and 125 mrad of inner ring rotated angle ($\theta_I$), correspond to contacts changing to zones of different mesh densities in the rolling direction, cf. Fig. 6b.

## 4.3. Equilibrium solutions for different operating conditions

Steady rolling equilibrium configurations of the roller have been computed with CECT for a range of normal loads and friction levels. The results are summarized in Fig. 17. Two distinct equilibrium configurations of the roller are observed. There is a first configuration, which is closer to the nominal roller position, feasible at higher loads. This will be identified here as configuration 1. The results shown in previous sections correspond to this configuration. On the other hand, there is a second configuration, feasible at lower loads. This will be identified here as configuration 2. With higher coefficients of friction $\mu$, there is a range of intermediate loads in which both configurations are feasible.

The second configuration is farther from the nominal roller position, with higher axial offsets (Fig. 17a), tilt and skew angles of the roller. This configuration also involves higher rolling torques and associated resultant longitudinal forces in each contact (Fig. 17b) and higher frictional powers (Fig. 17c). The transition loads from configuration 1 to configuration 2 increase as $\mu$ increases. Also, the leap between both configurations is higher for higher $\mu$.

Figures 18 and 19 illustrate a case of each configuration. The figures depict free-body diagrams of the roller, including the resultant tangential frictional forces and spin moments in each contact and the centres of the normal pressures marked with filled circles. The nominal contact positions are also shown with unfilled red circles. The frictional forces and moments are represented acting on these points on the roller.

**Table 2:** Frictional contact resultant forces on the roller and roller axial offset computed with CECT and FEM for $N = 5.5$ kN and $\mu = 0.10$ and 0.30.

| | $\mu = 0.10$ | | | $\mu = 0.30$ | | |
|---|---|---|---|---|---|---|
| | Full slip | CECT | FEM | Full slip | CECT | FEM |
| $f_{x,i}$ (–) | 4.36E–03 | –4.96E–03 | –4.8E–03 | 2.58E–02 | –5.33E–03 | –5.2E–03 |
| $f_{x,e}$ (–) | 7.31E–03 | 4.99E–03 | 4.8E–03 | –1.28E–02 | 5.33E–03 | 5.2E–03 |
| $f_{lat,i}$ (–) | –5.20E–03 | 2.23E–02 | 5.5E–04 | –1.08E–02 | 2.34E–02 | 1.3E–02 |
| $f_{lat,e}$ (–) | 5.63E–03 | 2.87E–02 | 5.7E–02 | 1.20E–02 | 3.22E–02 | 5.2E–02 |
| $\sum f_{lat}$ (–) | 4.54E–04 | 5.09E–02 | 5.8E–02 | 1.17E–03 | 5.55E–02 | 6.5E–02 |
| $d_y$ ($\mu$m) | - | 6.3 | 7.2 | - | 20.4 | 23.5 |

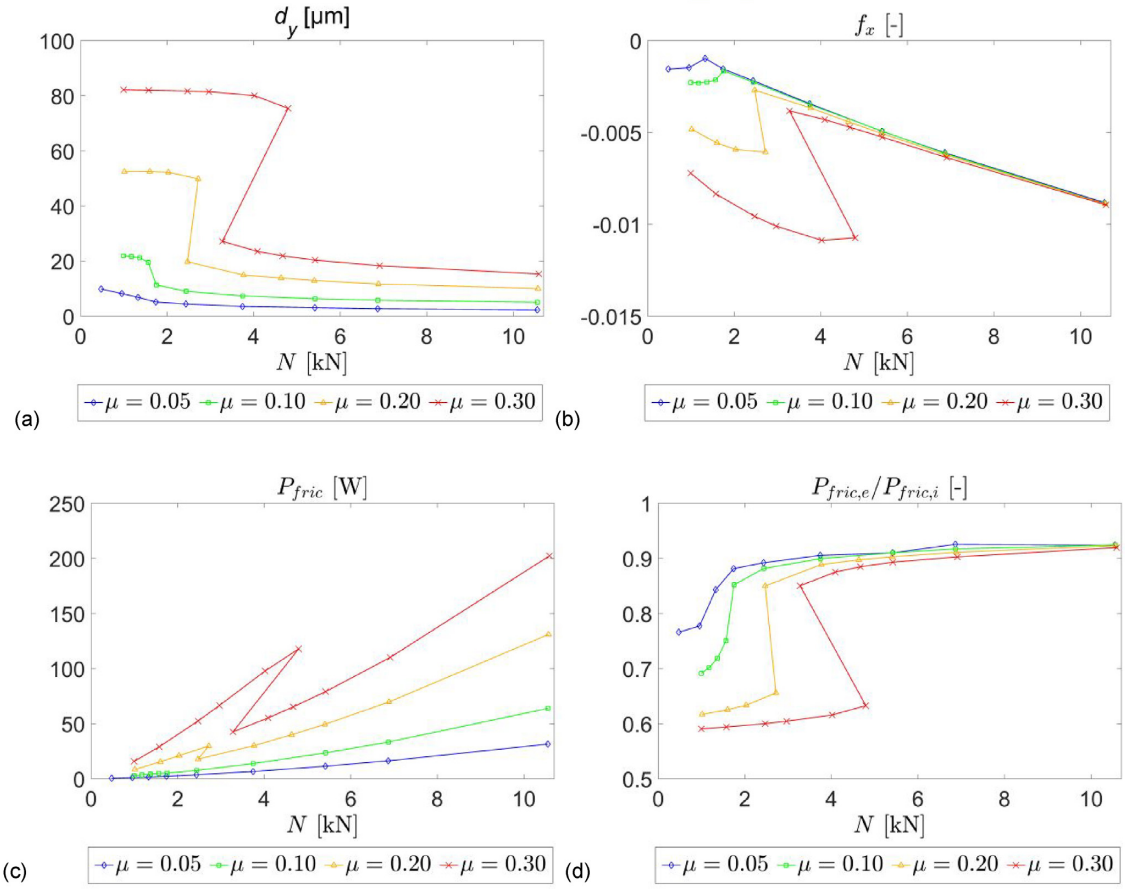


**Figure 17:** Steady rolling contact configurations of the roller computed with contact solutions of CECT for different normal loads and coefficients of friction. (a) Axial offset $d_y$ of the roller from its nominal position. (b) Longitudinal force in roller–race contacts $f_x = F_x/\mu N$. (c) Total dissipated power by friction in roller–race contacts, $P_{fric}$. (d) Ratio of frictional power in contact of roller with outer to inner race, $P_{fric,e}/P_{fric,i}$.

In equilibrium configuration 1, the resultant frictional lateral forces transmitted to the roller in both contacts have the same direction, as may be observed in Fig. 18a. The roller has a small axial displacement in the direction of these forces so that the contact centres are shifted in this direction, and an axial component of the normal forces appears to balance the lateral frictional forces. The lateral frictional forces are higher for higher $\mu$. As a result, the axial displacement of the roller in the equilibrium position is higher for higher $\mu$, and the rolling torques and frictional power increase somewhat more than proportionally with $\mu$.

For a given $\mu$, the axial displacement of the roller is higher at lower normal loads, cf. Fig. 17a. This is because the ratio of camber thrust to normal load increases at lower loads in this case. In non-conformal contact, this ratio remains constant for a given ellipticity of the contact patch, coefficient of friction, and spin. In this case, as the load increases, this ratio becomes smaller due to the higher friction saturation in the longitudinal direction, resulting from higher longitudinal rigid slip velocities. This effect is notable despite the modest total contact angle variation in the contact patch (approx. 11° with $N = 5.5$ kN) because the variation of the rolling radii is relatively high. This is a distinctive feature of conformal contact in rolling bearings with respect to conformal wheel–rail contact, as a result of the much higher ratios of lateral profile radii over rolling radii seen in this application.

Continuing with equilibrium configuration 1, the roller also adopts a small negative tilt, of the order of −0.05 mrad according to the computations with CECT (higher with higher $\mu$). The tilt

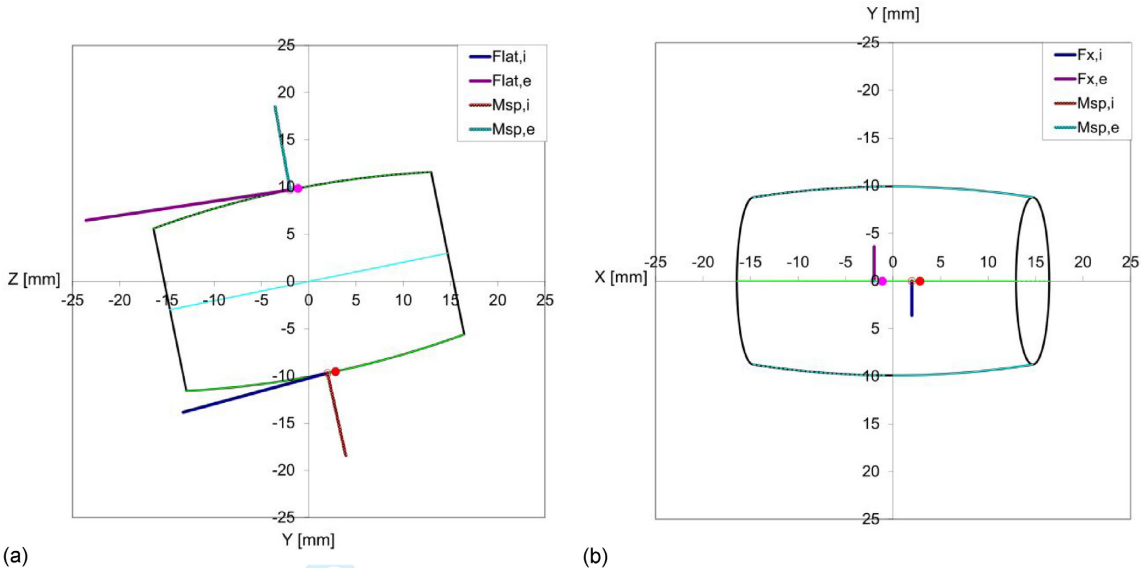


**Figure 18:** Roller free-body diagram in equilibrium configuration 1 with $N = 5.5$ kN and $\mu = 0.30$. (a) Front view. (b) Plan view.

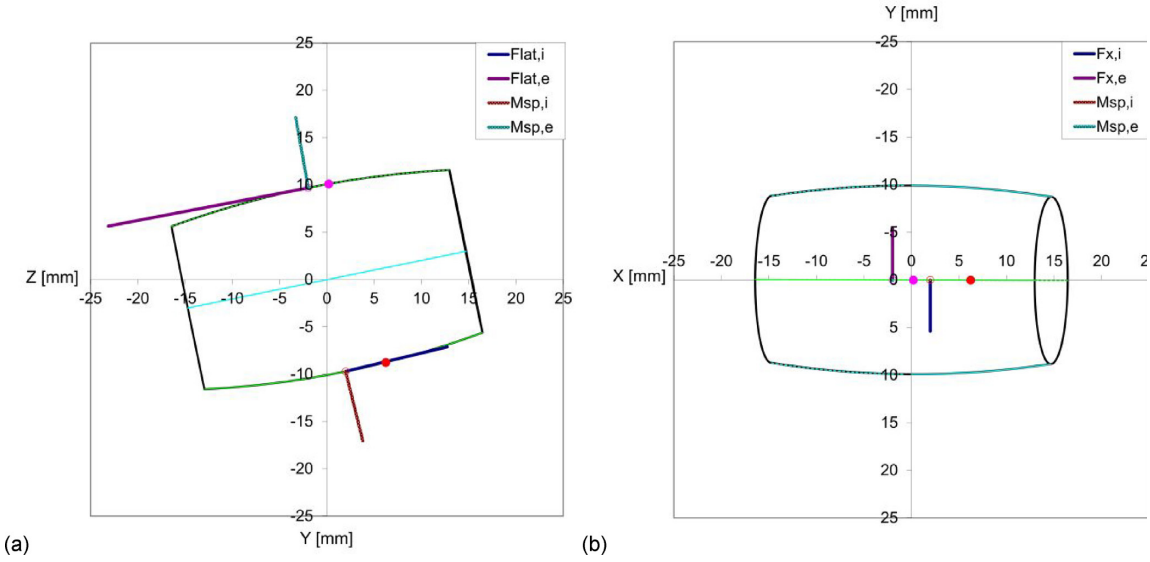


**Figure 19:** Roller free-body diagram in equilibrium configuration 2 with $N = 4$ kN and $\mu = 0.30$. (a) Front view. Note: the lateral forces have been scaled down by a factor of 10 in this view. (b) Plan view.

values computed with FEM are higher, cf. Fig. 15, possibly due to global deflections in the FE model. As a result of the negative tilt of the roller, the offset from the nominal position is slightly higher in the inner contact, and the inner normal load causes a higher moment along x than the outer. This is balanced by the difference in the lateral frictional forces of both contacts, being higher the outer one. The lateral frictional forces are greater than the longitudinal ones, as may be seen comparing Fig. 18a and b, in which the forces are represented at the same scale.

The roller axial offsets, tilt, and skew angles are much higher in equilibrium configuration 2. The skew angles increase up to –4 mrad, and the tilt angles increase up to about –0.4 mrad with $\mu = 0.3$. The offset of the inner contact from its nominal position is considerably higher than that of the outer contact, as may be seen in Fig. 19a, as a result of this increased tilt. The dissipated power in the inner contact also increases more than in the outer contact in this configuration, cf. Fig. 17d. The lateral frictional forces are much higher than in configuration 1, as may be seen comparing Fig. 19a with Fig. 18a. Note that the lateral forces have been scaled down by a factor of 10 in Fig. 19a; the scale of the rest of the forces and moments is the same in Figs. 18 and 19. The direction of the lateral frictional force of the inner contact is also reversed.

It has to be mentioned that in some cases in which equilibrium configuration 2 is found as the only one complying with steady equilibrium strictly, the force residuals with roller configurations that may be assimilated to equilibrium configuration 1 are not high. Also, the slow lateral movement of the roller when being out of its steady equilibrium position is recalled. Further research is necessary on the practical significance of equilibrium configuration 2.

The effects described here, as well as the lateral contact shifts shown in Section 4.1, are more relevant with higher coefficients of friction. A 3D partial slip contact model is necessary to capture

them, with the ability to predict lateral frictional forces in addition to the longitudinal ones, as well as moments related to both longitudinal and lateral contact stresses. The lateral frictional forces referred to here are the ones coming e.g., from spin in a contact with no lateral creepage, which full slip and 1D models fail to predict. At lower friction levels, such as may be found in well-lubricated conditions, the offsets of the roller from its nominal position are small, as may be seen in Fig. 17a. In this case, it may be satisfactory to assume nominal roller position and use a simpler contact mechanics model, e.g., the strip theory or the full slip solution.

The computation of the equilibrium configuration(s) of the roller for each combination of $N$ and $\mu$ has taken of the order of minutes to tens of minutes with CECT. Each of these equilibriums involves the computation of several pairs of inner/outer contact solutions, iterating with the six parameters defining the roller configuration as outlined in Section 3.2. The FEM described in Section 3.3 has much greater computational demands, with a single run taking about tens of hours in a high-performance computer. The application of this FEM in this study would be much less practical due to the high computational costs and the need to start from positions close to the sought equilibrium configuration, as illustrated in Section 4.2.

## 5. Conclusions

The roller–raceway frictional contact has been studied in a spherical roller bearing. For this purpose, different partial slip contact models have been used, as opposed to the usual full slip approach: the strip theory, an implementation of Kalker's exact contact theory called CECT, and FEM. The use of CECT, previously applied in wheel–rail contact, has been demonstrated in the contact analysis of a spherical roller bearing. The method may also be applied in other types of rolling bearings. The need for a variable discretization size $\Delta q$ is highlighted, due to the variable rolling radii of the contact surfaces. Regarding the FEM, it has been shown that a precise analysis of the motions of the roller is necessary to arrive at the solution corresponding to the steady rolling configuration of the roller. Also, in the presented FEM analyses, relatively long rolling distances, of the order of ten times the total longitudinal dimension of the contact patch, have been necessary to achieve reasonably stabilized solutions. These contrast with the much lower distances necessary to reach a quasi-steady state at the local contact level. The required rolling distances could be different in other cases or with other analysis set-ups.

The studied contact patches present a high width-to-length ratio, modest contact angle variations, and rigid slip velocities mostly aligned in the rolling direction. These features point to 2D-like contact solutions and anticipate that representative results may be obtained with strip theory. Indeed, the results obtained with the strip theory agree quite well with those obtained with the more comprehensive 3D contact models, as long as the contact patch position is appropriately adjusted. However, a 3D partial slip contact model is needed to perform this adjustment, with a proper description of the rigid slip velocities in the roller–raceway contacts according to the geometry of the non-planar contact surfaces, and the capability to compute lateral frictional forces in addition to the longitudinal ones, as well as associated moments. While the lateral frictional forces are relatively small in the studied short contact patches (as compared to the normal loads), with high friction, they may be high enough to cause a noticeable lateral shift of the contact patch with a roller having zero nominal roller angle. This lateral shift, in turn, influences the tangential contact solution. At lower friction levels, the frictional forces are smaller, and the contact shifts from their nominal positions have been shown to decrease in the studied bearing. Still, the relevance of possible contact shifts should be evaluated for each bearing geometry and operating conditions. These could come for reasons other than frictional forces, e.g., in the presence of internal clearances, axial loading, and misalignment.

The advantages and disadvantages of the different contact models considered in this work are summarized in the following points:

1. The strip theory may be used to get detailed steady-state contact solutions efficiently in cases with wide contact patches and slip velocities aligned in one direction, in which the contact location may be estimated beforehand, aside from the contact frictional forces.
2. The exact contact theory is a comprehensive 3D partial slip contact model that may be applied to get precise frictional contact solutions within the framework of linear elastostatics, providing a realistic representation of the effect of the contact frictional forces on the roller equilibrium. Its computational costs are between those of strip theory and FEM while allowing a much more general application than strip theory.
3. The main difficulty for the practical application of FEM in the type of contact problems treated here is its high computational costs. Its use should be reserved for studying phenomena not allowed by simpler contact models, such as non-linear material behaviour.

The steady rolling configurations of the roller have been computed for different normal loads and friction levels with the exact contact theory. Two different steady equilibrium configurations of the roller have been found. There is a first configuration, which may be described as the expected one, in which the roller has low or moderate offsets from its nominal position in the bearing radial plane. This configuration is feasible at higher loads. The second configuration, which is feasible at lower loads, presents higher roller offsets and dissipated powers. The leap between both configurations increases with higher friction levels. The finding of these two configurations in a numerical analysis requires using a 3D partial slip contact model. Further research is necessary on the significance of the second steady equilibrium configuration of the roller. For this purpose, it may be interesting to investigate the transient evolution of the roller in its orbital motion around the bearing.

## Acknowledgments

J.B.-L., J.S., and E.G.V. gratefully acknowledge financial support from the European Horizon 2020 Joint Technology Initiative Shift2Rail through contracts 826255 and 101012456 (IN2TRACK2 and IN2TRACK3), from the Spanish Research Ministry MICINN/Economy and Competitiveness Ministry MINECO and MCI/AEI through contract PID2019-109483RB-I00, including funding by the FEDER-ERDF European Regional Development Fund, and from the Basque Government through IT1764-22.

## References

Abascal, R., & Rodríguez-Tembleque, L. (2007). Steady-state 3D rolling contact using boundary elements. *Communications in Numerical Methods in Engineering*, **23**, 905–920. https://doi.org/10.1002/cnm.931.

Abdullah, M. U., Khan, Z. A., Kruhoeffer, W., & Blass, T. (2020). A 3D finite element model of rolling contact fatigue for evolved material response and residual stress estimation. *Tribol Letters*, **68**, 122. https://doi.org/10.1007/s11249-020-01359-w.

Baeza, L., Vila, P., Xie, G., & Iwnicki, S. D. (2011). Prediction of rail corrugation using a rotating flexible wheelset coupled with a flexible track model and a non-Hertzian/non-steady contact model. *Journal of Sound and Vibration*, **330**, 4493–4507. http://dx.doi.org/10.1016/j.jsv.2011.03.032.

Bass, J. M. (1987). Three-dimensional finite deformation, rolling contact of a hyperelastic cylinder: Formulation of the problem and computational results. *Computers & Structures*, **26**, 991–1004. https://doi.org/10.1016/0045-7949(87)90116-7.

Behnke, R., & Kaliske, M. (2015). Thermo-mechanically coupled investigation of steady state rolling tires by numerical simulation and experiment. *International Journal of Non-Linear Mechanics*, **68**, 101–131. https://doi.org/10.1016/j.ijnonlinmec.2014.06.014.

Blanco-Lorenzo, J., Santamaria, J., Vadillo, E. G., & Correa, N. (2016). On the influence of conformity on wheel-rail rolling contact mechanics. *Tribology International*, **103**, 647–667. https://doi.org/10.1016/j.triboint.2016.07.017.

Blanco-Lorenzo, J., Santamaria, J., Vadillo, E. G., & Correa, N. (2018). A contact mechanics study of 3D frictional conformal contact. *Tribology International*, **119**, 143–156. https://doi.org/10.1016/j.triboint.2017.10.022.

Blanco-Lorenzo, J., Vollebregt, E. A. H., Santamaria, J., & Vadillo, E. G. (2021). Approximating the influence coefficients of non-planar elastic solids for conformal contact analysis. *Tribology International*, **154**, 106671. https://doi.org/10.1016/j.triboint.2020.106671.

Bomidi, J. A. R., & Sadeghi, F. (2014). Three-dimensional finite element elastic-plastic model for subsurface initiated spalling in rolling contacts. *Journal of Tribology*, **136**, 011402. https://doi.org/10.1115/1.4025841.

Carter, F. W. (1926). On the action of a locomotive driving wheel. *Proceedings of the Royal Society of London, Series A*, **112**, 151–157. https://doi.org/10.1098/rspa.1926.0100.

Damme, S., Nackenhorst, U., Wetzel, A., & Zastrau, B. W. (2003). On the numerical analysis of the wheel–rail system in rolling contact. In K. Popp, & W. Schielen (Eds.), *System dynamics and long-term behavior of railway vehicles, track and subgrade* (pp. 155–174). Springer. https://doi.org/10.1007/978-3-540-45476-2_10.

Dassault Systèmes Simulia Corp.(2012). *Abaqus analysis user's manual, Version 6.12*.

Donea, J., Huerta, A., Ponthot, J. P., & Rodríguez-Ferran, A. (2004). Arbitrary Lagrangian–Eulerian methods. In E. Stein, R. Borst, & T. Hughes (Eds.), *Encyclopedia of computational mechanics, Vol. 1: Fundamentals* (pp. 413–437). Wiley. https://doi.org/10.1002/0470091355.ecm009.

Draganis, A. (2017). Finite element modelling of transient thermomechanical rolling contact featuring mixed control of the rigid body motion. *Journal of Tribology*, **139**, 011503. https://doi.org/10.1115/1.4033048.

Draganis, A., Larsson, F., & Ekberg, A. (2015). Finite element modelling of frictional thermomechanical rolling/sliding contact using an arbitrary Lagrangian–Eulerian formulation. *Proceedings of the Institution of Mechanical Engineers, Part J: Journal of Engineering Tribology*, **229**, 870–880. https://doi.org/10.1177/1350650115572197.

Fallahnezhad, K., Liu, S., Brinji, O., Marker, M., & Meehan, P. A. (2019). Monitoring and modelling of false brinelling for railway bearings. *Wear*, **424–5**, 151–164. https://doi.org/10.1016/j.wear.2019.02.004.

Faria, L. O., Bass, J. M., Oden, J. T., & Becker, E. B. (1989). A three-dimensional rolling contact model of a reinforced rubber tire. *Tire Science and Technology*, **17**, 217–233. https://doi.org/10.2346/1.2141686.

Faria, L. O., Oden, J. T., Yavari, B., Tworzydlo, W., Bass, J. M., & Becker, E. B. (1992). Tire modeling by finite elements. *Tire Science and Technology*, **20**, 33–56. https://doi.org/10.2346/1.2139507.

González, J. A., & Abascal, R. (1998). Using the boundary element method to solve rolling contact problems. *Engineering Analysis with Boundary Elements*, **21**, 385–392. https://doi.org/10.1016/S0955-7997(98)00026-5.

González, J. A., & Abascal, R. (2000). An algorithm to solve coupled 2D rolling contact problems. *International Journal for Numerical Methods in Engineering*, **49**, 1143–1167. https://doi.org/10.1002/1097-0207(20001130)49:9<1143::AID-NME991>3.0.CO;2-B

Haines, D. J., & Ollerton, E. (1963). Contact stress distributions on elliptical contact surfaces subjected to radial and tangential forces. *Proceedings of the Institution of Mechanical Engineers*, **177**, 95–114. https://doi.org/10.1243/PIME_PROC_1963_177_014_02.

Halling, J. (1966–67). Analysis of spin/roll conditions and the frictional-energy dissipation in angular-contact thrust ball bearings. *Proceedings of the Institution of Mechanical Engineers*, **181**, 349–362. https://doi.org/10.1243/PIME_PROC_1966_181_035_02.

Harris, T. A. (2001). *Rolling bearing analysis, ISBN 0-471-35457-0* (4th ed.). John Wiley & Sons, Inc.

Hartnett, M. J. (1979). The analysis of contact stresses in rolling element bearings. *Journal of Lubrication Technology*, **101**, 105–109. https://doi.org/10.1115/1.3453270.

Heras, I. (2018). Four-point contact slewing bearings for wind turbines: Advances in structural modelling and friction torque calculation. *PhD thesis*. University of the Basque Country.

Heras, I., Aguirrebeitia, J., & Abasolo, M. (2017b). Friction torque in four contact point slewing bearings: Effect of manufacturing errors and ring stiffness. *Mechanism and Machine Theory*, **112**, 145–154. https://doi.org/10.1016/j.mechmachtheory.2017.02.009.

Heras, I., Aguirrebeitia, J., Abasolo, M., & Plaza, J. (2017a). Friction torque in four-point contact slewing bearings: Applicability and limitations of current analytical formulations. *Tribology International*, **115**, 59–69. https://doi.org/10.1016/j.triboint.2017.05.011.

Houpert, L. (1999). Numerical and analytical calculations in ball bearings. In *Proceedings of the 8th European Space Mechanisms And Tribology Symposium*.

Houpert, L. (2002). Ball bearing and tapered roller bearing torque: Analytical, numerical and experimental results. *Tribology Transactions*, **45**, 345–353. https://doi.org/10.1080/10402000208982559.

Hu, H., & Wriggers, P. (2002). On the adaptive finite element method of steady-state rolling contact for hyperelasticity in finite deformations. *Computer Methods in Applied Mechanics and Engineering*, **191**, 1333–1348. https://doi.org/10.1016/S0045-7825(01)00326-7.

Jin, X., Wen, Z., Zhang, W., & Shen, Z. (2005). Numerical simulation of rail corrugation on a curved track. *Computers and Structures*, **83**, 2052–2065. http://dx.doi.org/10.1016/j.compstruc.2005.03.012.

Johnson, K. L. (1985). *Contact mechanics*. Cambridge University Press. https://doi.org/10.1017/CBO9781139171731.

Jones, A. B. (1959). Ball motion and sliding friction in ball bearings. *ASME Journal of Basic Engineering*, **81**, 1–12. https://doi.org/10.1115/1.4008346.

Ju, S. H., Horng, T. L., & Cha, K. C. (2000). Comparisons of contact pressures of crowned rollers. *Proceedings of the Institution of Mechanical Engineers, Part J: Journal of Engineering Tribology*, **214**, 147–156. https://doi.org/10.1243/1350650001543061.

Kabe, K., & Koishi, M. (2000). Tire cornering simulation using finite element analysis. *Journal of Applied Polymer Science*,

**78**, 1566–1572. https://doi.org/10.1002/1097-4628(20001121)78:8(1566::AID-APP140)3.0.CO;2-I.

Kaiser, I. (2012). Refining the modelling of vehicle-track interaction. *Vehicle System Dynamics*, **50**, 229–243. http://dx.doi.org/10.1080/00423114.2012.671948.

Kalker, J. J. (1979). The computation of three-dimensional rolling contact with dry friction. *International Journal for Numerical Methods in Engineering*, **14**, 1293–1307.

Kalker, J. J. (1982). A fast algorithm for the simplified theory of rolling contact. *Vehicle System Dynamics*, **11**, 1–13. https://doi.org/10.1080/00423118208968684.

Kalker, J. J. (1990). *Three-dimensional elastic bodies in rolling contact, Vol. 2 of solid mechanics and its applications*. Kluwer Academic Publishers. https://doi.org/10.1002/nme.1620140904.

Kalker, J. J. (2001). Rolling contact phenomena: Linear elasticity. Ch 1. In B. Jacobson, & J. J. Kalker (Eds.), *Rolling contact phenomena, CISM courses and lectures, 411*(pp. 1–84). Springer. https://doi.org/10.1007/978-3-7091-2782-7_1.

Karapetyan, A. V. (2009). A two-parameter friction model. *Journal of Applied Mathematics and Mechanics*, **73**, 367–370. https://doi.org/10.1016/j.jappmathmech.2009.08.016.

Kireenkov, A. A. (2008). Combined model of sliding and rolling friction in dynamics of bodies on a rough plane. *Mechanics of Solids*, **43**, 412–425. https://doi.org/10.3103/S0025654408030138.

Kleckner, R. J., & Pirvics, J. (1982). Spherical roller bearing analysis. *Journal of Lubrication Technology*, **104**, 99–108. https://doi.org/10.1115/1.3253170.

Kudra, G., & Awrejcewicz, J. (2013). Approximate modelling of resulting dry friction forces and rolling resistance for elliptic contact shape. *European Journal of Mechanics: A/Solids*, **42**, 358–375. https://doi.org/10.1016/j.euromechsol.2013.07.005.

Laursen, T. A., & Stanciulescu, I. (2006). An algorithm for incorporation of frictional sliding conditions within a steady state rolling framework. *Communications in Numerical Methods in Engineering*, **22**, 301–318. https://doi.org/10.1002/cnm.815.

Le Tallec, P., & Rahier, C. (1994). Numerical models of steady rolling for non-linear viscoelastic structures in finite deformations. *International Journal for Numerical Methods in Engineering*, **37**, 1159–1186. https://doi.org/10.1002/nme.1620370705.

Leblanc, A., & Nelias, D. (2007). Ball motion and sliding friction in a four-contact-point ball bearing. *Journal of Tribology*, **129**, 801–808. https://doi.org/10.1115/1.2768079.

Legrand, E., & Mondier, J. B. (1995). Estimation of friction torque in solid lubricated ball bearings. In *Proceedings of the 6th European Space Mechanisms and Tribology Symposium*.

Leine, R. I., & Glocker, Ch. (2003). A set-valued force law for spatial Coulomb–Contensou friction. *European Journal of Mechanics: A/Solids*, **22**, 193–216. https://doi.org/10.1016/S0997-7538(03)00025-1.

Li, F., Hu, W., Meng, Q., Zhan, Z., & Shen, F. (2018). A new damage-mechanics-based model for rolling contact fatigue analysis of cylindrical roller bearing. *Tribology International*, **120**, 105–114. https://doi.org/10.1016/j.triboint.2017.12.001.

Li, Z. (2002). *Wheel-rail rolling contact and its application to wear simulation*. Ph.D. dissertation. Technische Universiteit Delft.

Li, Z., Zhao, X., Esveld, C., Dollevoet, R., & Molodova, M. (2008). An investigation into the causes of squats—Correlation analysis and numerical modeling. *Wear*, **265**, 1349–1355. https://doi.org/10.1016/j.wear.2008.02.037.

Lin, C.-L., & Meehan, P. A. (2021). Morphological and elemental analysis of wear debris naturally formed in grease lubricated railway axle bearings. *Wear*, **484–5**, 203994. https://doi.org/10.1016/j.wear.2021.203994.

Liu, S., Wang, Q., & Liu, G. (2000). A versatile method of discrete convolution and FFT (DC-FFT) for contact analyses. *Wear*, **243**, 101–111. https://doi.org/10.1016/S0043-1648(00)00427-0.

Meehan, P. A., Milne, C. D., & Liu, S. (2017). Investigation of wear degradation of railway spherical roller bearings. In *Proceedings of the 25th International Symposium on Dynamics of Vehicles on Roads And Tracks (IAVSD 2017)*. https://doi.org/10.1201/9781351057189.

Nackenhorst, U. (1993). On the finite element analysis of steady state rolling contact. In M. H. Aliabadi, & C. A. Brebbia (Eds.), *Contact mechanics—Computational techniques* (pp. 241–248). Computational Mechanics Publication.

Nackenhorst, U. (2004). The ALE-formulation of bodies in rolling contact. Theoretical foundations and finite element approach. *Computer Methods in Applied Mechanics and Engineering*, **193**, 4299–4322. https://doi.org/10.1016/j.cma.2004.01.033.

Nackenhorst, U., Zastrau, B. W., & Jarewski, J. (2000). Finite element modelling of 3D elastic–elastic rolling contact. *Zeitschrift für Angewandte Mathematik und Mechani*, **80**, 57–60. https://doi.org/10.1002/zamm.20000801315.

Oden, J. T., & Lin, T. L. (1986). On the general rolling contact problem for finite deformations of a viscoelastic cylinder. *Computer Methods in Applied Mechanics and Engineering*, **57**, 297–367. https://doi.org/10.1016/0045-7825(86)90143-X.

Oden, J. T., Lin, T. L., & Bass, J. M. (1988). A finite element analysis of the general rolling contact problem for a viscoelastic rubber cylinder. *Tire Science and Technology*, **16**, 18–43. https://doi.org/10.2346/1.2148795.

Oh, K. P., & Trachman, E. G. (1976). A numerical procedure for designing profiled rolling elements. *Journal of Lubrication Technology*, **98**, 547–551. https://doi.org/10.1115/1.3452922.

Oloffson, U., Andersson, S., & Björklund, S. (2000). Simulation of mild wear in boundary lubricated spherical roller thrust bearings. *Wear*, **241**, 180–185. https://doi.org/10.1016/S0043-1648(00)00373-2.

Padovan, J. (1987). Finite element analysis of steady and transiently moving/rolling nonlinear viscoelastic structure—I. Theory. *Computers & Structures*, **27**, 249–257. https://doi.org/10.1016/0045-7949(87)90093-9.

Padovan, J., Tovichakchaikul, S., & Zeid, I. (1984). Finite element analysis of steadily moving contact fields. *Computers & Structures*, **18**, 191–200. https://doi.org/10.1016/0045-7949(84)90119-6.

Panagiotopoulos, P. D. (1975). A nonlinear programming approach to the unilateral contact-, and friction-boundary value problem in the theory of elasticity. *Ingenieur-Archiv*, **44**, 421–432. https://doi.org/10.1007/BF00534623.

Pletz, M., Daves, W., Yao, W., & Ossberger, H. (2014). Rolling contact fatigue of three crossing nose materials—Multiscale FE approach. *Wear*, **314**, 69–77. https://doi.org/10.1016/j.wear.2013.11.013.

Pozzebon, M. L., Lin, C.-L., & Meehan, P. A. (2020). On the modeling of wear in grease-lubricated spherical roller bearings. *Tribology Transactions*, **63**, 806–819. https://doi.org/10.1080/10402004.2020.1743400.

Rafei, M., Ghoreishy, M. H. R., & Naderi, G. (2018). Computer simulation of tire rolling resistance using finite element method: Effect of linear and nonlinear viscoelastic models. *Proceedings of the Institution of Mechanical Engineers, Part D: Journal of Automobile Engineering*, **233**, 1–15. https://doi.org/10.1177/0954407018804117.

Rodríguez-Tembleque, L., & Abascal, R. (2010). A 3D FEM–BEM rolling contact formulation for unstructured meshes. *International Journal of Solids and Structures*, **47**, 330–353. https://doi.org/10.1016/j.ijsolstr.2009.10.008.

Schwack, F., Prigge, F., & Poll, G. (2018). Finite element simulation and experimental analysis of false brinelling and fretting corrosion.

*Tribology International*, **126**, 352–362. https://doi.org/10.1016/j.triboint.2018.05.013.

Schwack, F., Schneider, V., Wandel, S., de la Presilla, R. J., Poll, G., & Glavatskih, S. (2021). On the critical amplitude in oscillating rolling element bearings. *Tribology International*, **163**, 107154. https://doi.org/10.1016/j.triboint.2021.107154.

Slack, T., & Sadeghi, F. (2010). Explicit finite element modelling of subsurface initiated spalling in rolling contacts. *Tribology International*, **43**, 1693–1702. https://doi.org/10.1016/j.triboint.2010.03.019.

Suwannachit, A., & Nackenhorst, U. (2013). A novel approach for thermomechanical analysis of stationary rolling tires within an ALE-kinematic framework. *Tire Science and Technology*, **41**, 174–195. https://doi.org/10.2346/tire.13.410304.

Tonazzi, D., Komba, E. H., Massi, F., Le Jeune, G., Coudert, J. B., Maheo, Y., & Berthier, Y. (2017). Numerical analysis of contact stress and strain distributions for greased and ungreased high loaded oscillating bearings. *Wear*, **376–7**, 1164–1175. https://doi.org/10.1016/j.wear.2016.11.037.

Toumi, M., Chollet, H., & Yin, H. (2016). Finite element analysis of the frictional wheel–rail rolling contact using explicit and implicit methods. *Wear*, **366–367**, 157–166. https://doi.org/10.1016/j.wear.2016.06.008.

Vo, K. D., Tieu, A. K., Zhu, H. T., & Kosasih, P. B. (2014). A 3D dynamic model to investigate wheel–rail contact under high and low adhesion. *International Journal of Mechanical Sciences*, **85**, 63–75. https://doi.org/10.1016/j.ijmecsci.2014.05.007.

Vollebregt, E. A. H. (2010). Improving the speed and accuracy of the frictional rolling contact model "CONTACT". In B. H. V. Topping, J. M. Adam, F. J. Pallarés, R. Bru, & M. L. Romero (Eds.), *Proceedings of the 10th International Conference on Computational Structures Technology* (pp. 1–15). Civil-Comp Press. https://doi.org/10.4203/ccp.93.17.

Vollebregt, E. A. H. (2012). 100-fold speed-up of the normal contact problem and other recent developments in "CONTACT". In *Proceedings of the 9th International Conference on Contact Mechanics and Wear of Rail/Wheel Systems (CM2012)*.

Vollebregt, E. A. H. (2020). Detailed wheel/rail geometry processing using the planar contact approach. *Vehicle System Dynamics*, **60**, 1253–1291. https://doi.org/10.1080/00423114.2020.1853180.

Vollebregt, E. A. H. (2021). Detailed wheel/rail geometry processing using the conformal contact approach. *Multibody System Dynamics*, **52**, 135–167. https://doi.org/10.1007/s11044-020-09762-w.

Vollebregt, E. A. H. (2022). *User guide for CONTACT, rolling and sliding contact with friction. Technical report 20-01, version 22.1, Vtech CMCC*. www.kalkersoftware.org.

Vollebregt, E., & Segal, A. (2014). Solving conformal wheel-rail rolling contact problems. *Vehicle System Dynamics*, **51**, 455–468. http://dx.doi.org/10.1080/00423114.2014.906634.

Wang, G., & Knothe, K. (1993). Stress analysis for rolling contact between two viscoelastic cylinders. *Journal of Applied Mechanics*, **60**, 310–317. https://doi.org/10.1115/1.2900794.

Wang, Z., Jin, X., Keer, L. M., & Wang, Q. (2012). A numerical approach for analyzing three-dimensional steady-state rolling contact including creep using a fast semi-analytical method. *Tribology Transactions*, **55**, 446–457. http://dx.doi.org/10.1080/10402004.2012.667518.

Wollny, I., Hartung, F., & Kaliske, M. (2016). Numerical modeling of inelastic structures at loading of steady state rolling. Thermomechanical asphalt pavement computation. *Computational Mechanics*, **57**, 867–886. https://doi.org/10.1007/s00466-016-1266-2.

Wriggers, P. (2001). Finite element methods for rolling contact. Ch 2. In B. Jacobson, & J. J. Kalker (Eds.), *Rolling contact phenomena, CISM courses and lectures, 411* (pp. 85–162). Springer. https://doi.org/10.1007/978-3-7091-2782-7_2.

Zeid, I., & Padovan, J. (1981). Finite element modeling of rolling contact. *Computers & Structures*, **14**, 163–170. https://doi.org/10.1016/0045-7949(81)90098-5.

Zhao, X., & Li, Z. (2011). The solution of frictional wheel–rail rolling contact with a 3D transient finite element model: Validation and error analysis. *Wear*, **271**, 444–452. https://doi.org/10.1016/j.wear.2010.10.007.

Zhao, X., Wen, Z., Zhu, M., & Jin, X. (2014). A study on high-speed rolling contact between a wheel and a contaminated rail. *Vehicle System Dynamics*, **52**, 1270–1287. https://doi.org/10.1080/00423114.2014.934845.

Zhuravlev, V. (1998). The model of dry friction in the problem of the rolling of rigid bodies. *Journal of Applied Mathematics and Mechanics*, **62**, 705–710. https://doi.org/10.1016/S0021-8928(98)00090-2.

Ziefle, M., & Nackenhorst, U. (2008). Numerical techniques for rolling rubber wheels: Treatment of inelastic material properties and frictional contact. *Computational Mechanics*, **42**, 337–356. https://doi.org/10.1007/s00466-008-0243-9.

Zobova, A. A. (2019). Dry friction distributed over a contact patch between a rigid body and a visco-elastic plane. *Multibody System Dynamics*, **45**, 203–222. https://doi.org/10.1007/s11044-018-09637-1.